Controlling differentiation of stem cells via bioactive disordered cues

Yujie Zhang, Murielle Rémy, Evgeny Apartsin, Emilie Prouvé, Cécile Feuillie, Christine Labrugère, Nithavong Cam, Marie-Christine Durrieu

ARTICLE

Controlling Differentiation of Stem Cells via Bioactive Disordered Cues

Received 00th January 20xx,
Accepted 00th January 20xx

DOI: 10.1039/x0xx00000x

Yujie Zhang [a], Murielle Remy [a], Evgeny Apartsin [a], Emilie Prouvé [a], Cécile Feuillie [a], Christine Labrugere [b], Nithavong Cam [b], Marie-Christine Durrieu [a*]

Ideal bone tissue engineering is to induce bone regeneration through the synergistic integration of biomaterial scaffolds, bone progenitor cells, and bone-forming factors. Biomimetic scaffolds imitate the native extracellular matrix (ECM) and are often utilized in vitro as analogues of the natural ECM to facilitate investigations of cell-ECM interactions and processes. In vivo, the cellular microenvironment has a crucial impact on regulating cell behavior and functions. PET surface was activated and then functionalized with mimetic peptides to promote human mesenchymal stem cell (hMSC) adhesion and differentiation into osteogenic lineage. A spray technology was assessed to randomly micropattern peptides (RGD and BMP-2 mimetic peptides) on PET surface. The distribution of the peptides grafted on the surface, the roughness of the surfaces and the chemistry of the surfaces at each step of the treatment were ascertained by Atomic Force Microscopy, fluorescence microscopy, Time-of-flight secondary ion mass spectrometry, Toluidine Blue O assay, and X-ray Photoelectron Spectroscopy. Subsequently, cell lineage differentiation was evaluated by quantifying the expression of immunofluorescence markers: osteoblast markers (Runx-2, OPN) and osteocyte markers (E11, DMP1, and SOST). In this article, we hypothesized that a unique combination of bioactive micro/nanopatterns onto polymer surface improves the rate of morphology change and enhance the hMSC differentiation. In DMEM medium, after 14 days, disordered micropatterned surfaces with RGD and BMP-2 led to a higher osteoblast marker expression than surfaces with a homogenously dual peptide conjugation. Finally, hMSC cultured in osteogenic differentiation medium (ODM) accelerated cells' differentiation. In ODM, our results highlighted the expression of osteocyte markers when hMSCs were seeded on PET surfaces with random micropatterns.

Introduction

Stem Cells (SCs) are involved in the structuration or regeneration of all body tissues and have numerous foreseen applications in tissue engineering.[1-3] Mesenchymal stem cells (MSCs), multipotent cells, have been widely used in experimental cell therapy and tissue engineering because of their ability to differentiate into various lineages such as cartilage cells (chondrocytes), bone cells (osteoblasts), fat cells (adipocytes), or muscle cells (myocytes). An overview of the clinical status of relevant MSCs is available through the public clinical trials database (http://clinicaltrials.gov).[4, 5] There are currently 9,572 cell-based clinical trials, of which 1,141 are MSC-based projects. There are 93 items based on MSC for treating bone diseases and 9 for bone repair. Many of these completed trials demonstrated the safety and efficacy of MSC.[1, 6]

Recent advances in tissue engineering and regenerative medicine are based on protocols inducing *ex vivo* stem cell differentiation of MSCs before *in vivo* transplantation. However, *ex vivo* production of clinically relevant quantities of differentiated functional cells remains problematic in such tissue engineering applications. Indeed, the scarcity of MSCs coupled with inefficient differentiation protocols makes it currently difficult to obtain usable tissue and organoids. It has been shown that the stem cell microenvironment (biochemical, topographical & mechanical features) impacts the differentiation yield.[7, 8] The microenvironments surrounding stem cells are structurally complex, which renders experiments to explore the effects of this structure on cell function difficult. Thus, it is not trivial to independently vary and control biophysical and biochemical properties, making it challenging to study the impact of, for example, various micro and nano-environmental biochemical properties on stem cell function.

One strategy to efficiently induce cell differentiation involves integrating bioactive principles that favor stem cell adhesion and differentiation, which are naturally present in the extracellular matrices (ECM) and have a crucial role.[9] The ECM provides nutrients and growth factors that stimulate cell proliferation, migration, differentiation, and maturation, resulting in functional tissue. Stem Cells (SC) reside in a niche of neighboring cells, and the ECM is infused with autocrine and paracrine soluble growth factors.[10] Cellular behavior depends on the abundance and distribution of

[a.] *Univ. Bordeaux, CNRS, Bordeaux INP, CBMN, UMR 5248, F-33600 Pessac, France*
[b.] *Univ. Bordeaux, CNRS, PLACAMAT, UAR 3626, F-33600 Pessac, France*
Electronic Supplementary Information (ESI) available: [details of any supplementary information available should be included here]. See DOI: 10.1039/x0xx00000x

bioactive factors in the ECM, [9,] which undergoes remodeling as a result of cell self-renewal and differentiation.[11, 12] For instance, during MSCs proliferation, the native ECM has a higher concentration in fibroblast growth factor-2 (FGF-2), [12] while the ECM is richer in bone morphogenic protein-2 (BMP-2) during osteogenic differentiation.

The interplay between SCs and these components seems rather intricate, and SC-ECM interactions are extensively studied.[13, 14] During the past decade, cell-material interactions have emerged as a leading research area in regenerative medicine.[1, 4, 15, 16] Material scientists, including our group,[9, 17-31] have been designed a variety of biomimetic materials to reproduce cell-ECM interactions.[32, 33] Cellular behaviors are influenced by chemical cues, such as chemical composition,[9, 17-24, 27, 30, 31, 33-37] and ligand density.[38] Based on this knowledge, many strategies which translate native ECM features to *in vitro* models use growth factors to control the fate of MSCs.[39, 40]

Biochemical cues are the most explored and best-characterized stimuli. Their distribution and abundance within the native ECM depend on the type of the targeted cell response as well as the location of stem cell niche.[12] Bioactive factors can be spatially patterned onto synthetic surfaces using micro-contactor inkjet.[18, 41-46] As an example, photolithography offers an efficient and convenient method to generate protein micropatterns on any substrate. In this technique, the substrate is first uniformly coated with a photoresist.[47-49] This homogenous coat is then precisely etched by UV light source and a photomask to allow specific immobilization of the protein of interest.[50-53] While broadly adopted, this method has the inconvenient feature that each time one wants to make a novel micropattern, a new mask has to be manufactured by adding cost and time to the scientific process. In addition, only flat materials can be used. Multiprotein micropatterning is much more tedious to achieve with masks or protein stamps due to difficulties in alignment.[54 55]

Wang et al. studied how to obtain gold nanoarrays on glass by block copolymer micellar nanolithography to fabricate RGD micro/nano patterns onto a bioinert poly(ethylene glycol) (PEG) hydrogel surface. [56] Their group proposed a new point of view: not only peptide nanospacing but also cell size impact on cell differentiation. However, this is the first time someone compared separately the impact of these two factors on stem cell differentiation. The results reveal that RGD nanospacing, independent of cell spreading size, acts as a potent regulator of cell tension and stem cell differentiation. So far, no definitive conclusions about stem cell differentiation can be drawn based on micropatterning or nanopatterning alone. Padiolleau *et al*. used photolithography technique to synthesize bioactive micropatterned polymers on PET to mimic the microenvironment of stem cells in the ECM.[35, 36] RGD and BMP-2 mimetic peptides were combined according to different shapes (squares, rectangles, hexagons) or different square sizes (from 100 x 100 μm^2 to 25 x 25μm^2). Potential changes in hMSC phenotype seeded on bioactive micropatterned surfaces with different-sized square patterns were assessed by RT-qPCR. Not only the patterns geometry but also the bioactivity of the surfaces (one or two peptides were immobilized onto PET surfaces) significantly impacted on the differentiation of hMSCs into an osteoblastic lineage. Matthew et al. highlighted the effect of MSCs differentiation by cells on random nano topologies *vs* on highly ordered nano topologies. [57] In this work, they used electron beam lithography (EBL) to fabricate five different patterns on polymethylmethacrylate (PMMA), all with a center-to-center spacing of 300 nm. These patterns were square array, hexagonal array, disordered square array with dots displaced randomly by up to 50 nm on both axes from their position in a square (DSQ50), disordered square array with dots displaced randomly by up to 20 nm on both axes from their position in a square (DSQ20), pits placed randomly over a 150 µm by 150 µm field, repeated to fill a 1 cm^2 area (RAND). After 21 days, MSCs on RAND had a more typical polygonal osteocyte morphology, while DSQ20 had typical osteoblast morphology and expressed OPN foci. These results showed that highly ordered nanotopographies produce negligibly low cell adhesion and osteoblast differentiation. However, cells on random nanotopography exhibited a more osteoblast morphology. Crucially, they showed that a novel nanodisplaced topography significantly increases bone-specific differentiation. This enhanced differentiation suggests that random cues may be an effective strategy to favour the differentiation of MSCs into bone cells for regenerative medicine and tissue engineering. [57]

Here, we describe a method to enable random micro or nanopatterning of any protein/peptide onto a 2D or 3D scaffold, which can be envisaged using spray technology. Our goal is to provide a new insight into the impact of the arrangement of bioactive micropatterns (ordered *vs* disordered) on the surface to control stem cell differentiation.[58, 59] Our spray technology allows to cover 2D or 3D scaffolds with controlled size and shape of bioactive micropatterns in a time-effective and economical manner at low cost.[60] To investigate the effects of density and distribution of adhesion and differentiation ligands on the osteoblastic differentiation of MSCs, Polyethylene terephthalate (PET) was used as a model material. RGD and BMP-2 mimetic peptides were used to favour MSC adhesion and differentiation into an osteoblast lineage, respectively.[19 61, 62] As extracellular matrix-derived peptides, they are both involved in a synergic manner in MSC osteogenic differentiation.[9, 56]

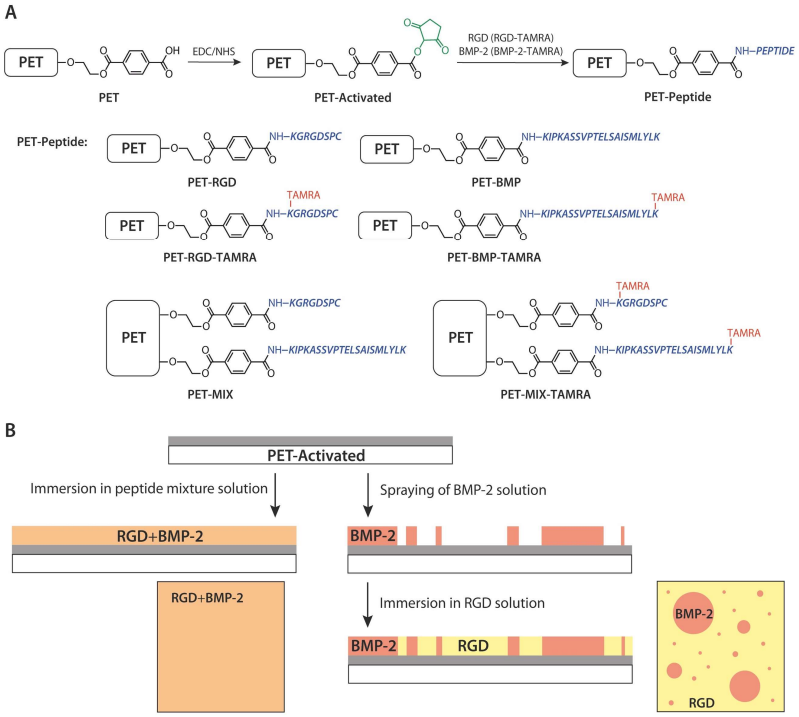

Figure 1. Peptide immobilization onto PET surfaces: A) PET functionalization with different peptides: PET-RGD, PET-BMP, PET-RGD-TAMRA, PET-BMP-TAMRA, PET-MIX, PET-MIX-TAMRA; B) Schematic drawing of PET micropatterning approaches.

In the present study, we synthesized micro, nanopatterned PET with different bioactive pattern size, surface coverage, and pattern shape. The bioactive surfaces were carefully characterized by Toluidine Blue test (TBO), X-ray photoelectron spectroscopy (XPS), Atomic Force Microscopy (AFM)), fluorescence microscopy and time-of-flight secondary ion mass spectrometry (ToF-SIMS). Immunocytochemical analysis allowed the evaluation of expression of markers related to osteogenic differentiation of hMSCs, namely Runx2, expressed during early osteoblast differentiation, osteopontin (OPN), expressed in late osteoblast differentiation, E11 and DMP-1, expressed in early stage of hMSC differentiation into osteocytes and SOST, expressed in late stage of hMSC differentiation into osteocytes.

Results

Evaluation of carboxyl density by using Toluidine Blue assay

Toluidine blue O (TBO) was used to determine the carboxyl group density onto PET surface after different modification steps. The absorbance of desorbed dyes in the solution allowed us to assess surface carboxyl groups' density onto PET surface.[63] COOH densities obtained for PET, PET-activated, PET-BMP and PET-RGD are 30 ± 7 pmol/mm^2 (~18 COOH/nm^2), 20 ± 8 pmol/mm^2 (~12 COOH/mm^2), 13 ± 0 pmol/mm^2 (~8 COOH/mm^2) and 17 ± 7 pmol/mm^2 (~10 COOH/nm^2) respectively.

XPS

The chemical compositions on each surface were evaluated by XPS. The XPS results indicate that PET is composed of atomic C (72.2%) and O (27.7%) (Table 2). The experimental C/O ratio is 2.6, close to the theoretical value of 2.5 taking into account which is challenging to avoid surface contamination from atmosphere. This result is consistent with previous publications (C=71.0 at.%, O=27.0 at.%, C/O=2.6).[36, 63] A slight contamination of nitrogen (N= 0.1 at.%) was detected on the PET surface. As reported by Fang et al., the components of PET mainly exist in C-C/C-H (284.8 eV), C-O (286.4 eV), and O-C=O (288.8 eV) bonding. In addition, the faint C1s peak generated by the benzene ring-related π-π* oscillation process in PET has the highest binding energy.[64]

Figure 2A shows the fitted C1s spectra is based on five components: C-C at 284.8 eV, C-CO at 285.2 eV, C-O at 286.5 eV, and O-C=O at 288.9 eV, π-π* at 291.3 eV (carbon bonding proportions are displayed in Table 2 and Fig. 2A). In addition, the ratio of C-C/COOR, C-CO/COOR, C-O/COOR, and O-C=O/COOR peak area is 2.4, 1.0, 1.1, 1.0 respectively, which is consistent with the chemical characteristics of PET. As expected for PET-Activated materials, nitrogen was 1.7% (Table 2). A new component at around 287.3 eV is required for fitting (Fig. 2A); therefore, assigned to the N–C=O bonds due to the NHS ester generated after the activation reaction, thus showing a surface modification efficiency. After EDC-NHS grafting, $C/N_{PET\text{-}Activated}$ was 42.2 (Table 2) with a slight decrease in oxygen content (i.e., O_{PET}=27.7 at. % vs. $O_{PET\text{-}Activated}$=26.5 at. %).

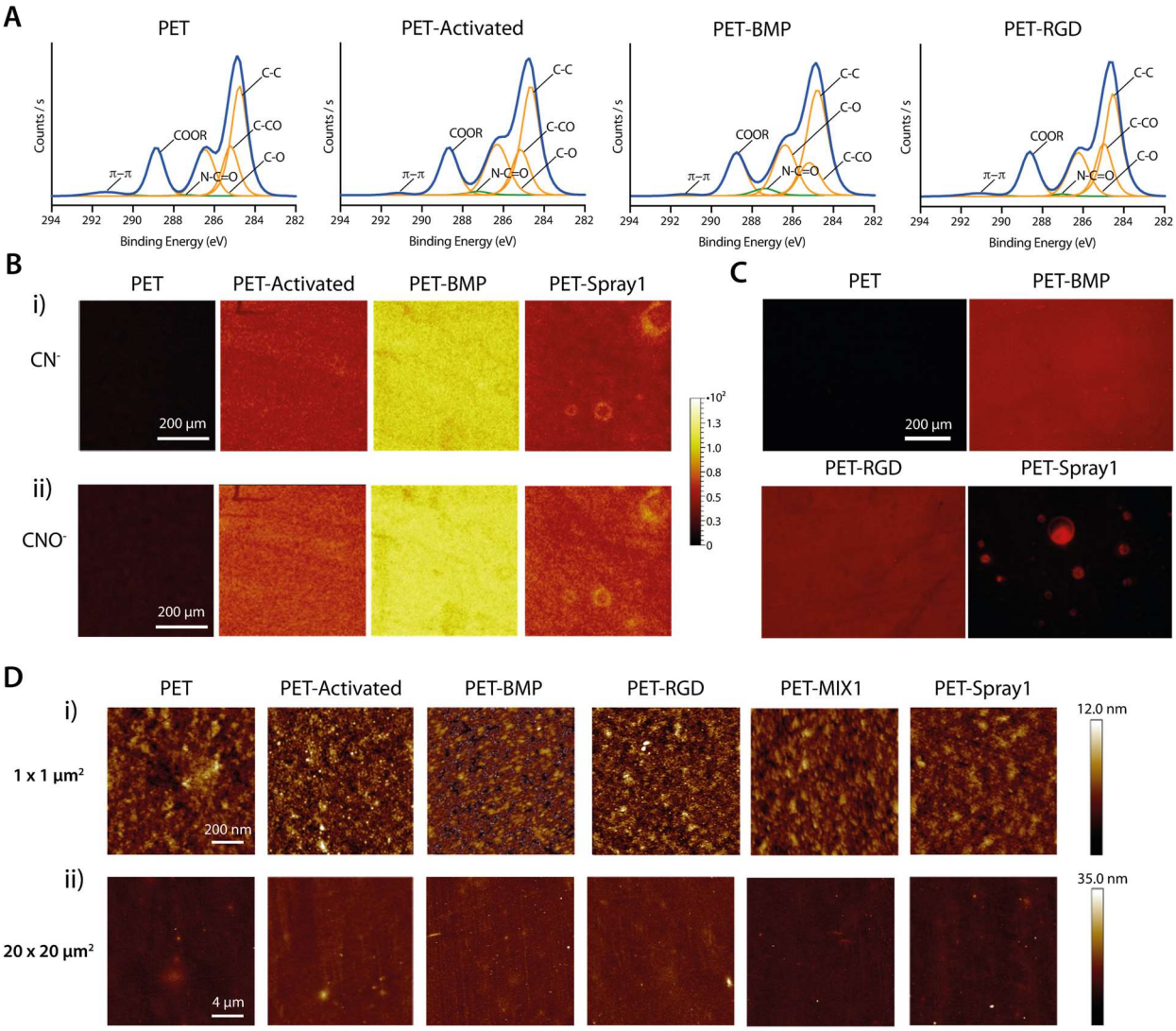

Figure 2. Characterizations of peptide immobilization onto PET surfaces A) Fitted C1s XPS spectra of PET, PET-Activated, PET-BMP, and PET-RGD; B) ToF-SIMS surface mapping of CN^- (B, i) and CNO^- (B, ii) ions on PET, PET-Activated, PET-BMP, PET-Spray. scale bar: 100 µm; C) Fluorescence microscopy images of RGD-TAMRA (in red) and BMP-2 -TAMRA (in red) grafted onto PET after sonication, scale bar: 200 µm; C) AFM height images measured after the different surface modification steps; obtained with a scanned area of 20 µm×20 µm (D, i), and 1 µm×1 µm (D, ii) from PET, PET-Activated, PET-BMP, PET-RGD, PET-Mix1, PET-Spray1.

Following the grafting peptide (Fig. 2A), the C1s spectra provide evidence of a slight increase of the characteristic peptide bond N–C=O at 287.3 eV and a slight decrease of C-O and O–C=O environments. Considering PET-BMP, N-C=O represent 2.2% carbon proportion vs. 1.1% for PET-activated (Table 2), and O–C=O represent 11.3% carbon proportion vs. 12.4% for PET-activated. The smallest peptides RGD (7 amino acid residues)[4] exhibit the lowest nitrogen composition (1 at. %) and the highest C/N ratio value equal to 72.4 (Table 2). In contrast, the surface grafted with the longest peptide BMP-2 (22 amino acid residues) gives the highest nitrogen content 2.6 at. %, and the lowest C/N ratio of 27.5.

ToF-SIMS

ToF-SIMS is a surface-sensitive analytical method.[65, 66] Figure 2B shows the surface images of CN^- at m/z 26 and CNO^- at m/z 42 after different modification steps. For experimental comparability, all samples were carried out under the same conditions, time, and the intensity level of CN^- and CNO^-.

Figure S2 shows the high mass resolution spectra of ToF-SIMS. The ToF-SIMS negative spectra (m/z 25 - m/z 175) of PET can provide us with information on the composition of PET. To study the surface composition properties of the materials more precisely after different modification steps, we focused on high mass resolution spectra from m/z 25 to m/z 50 (Fig. S2). Typically, we set the Y-axis as the signal intensity or ion count and the X-axis as the m/z plot. The height of the signal is proportional to the number of ions present in the spectrum. And the m/z of an ion is the mass of that ion. The material can determine the material's molecular formula by measuring the exact mass of the ions or the m/z difference between

ions. S2 observes $C_7H_5O_2^-$ at m/z 121 and $C_8H_4O_4^-$ at m/z 165. And these two fragment ions ($C_7H_5O_2^-$ and $C_8H_4O_4^-$) are specific peaks belonging to the typical polymer PET ($(C_{10}H_8O_4)_n$).[67, 68] Then, the PET surface was activated by EDC/NHS to obtain PET-Activated. This activation modification introduced NHS esters to PET (Fig. 2B). Therefore, the characteristic ions of nitrogen-containing functional groups (CN^-, CNO^-) can be detected in the high mass resolution spectra of PET-Activated.[69]

At first sight, we can observe that PET is homogenously black, PET-Activated is homogenously red, and PET-BMP-2-TAMRA is homogenously yellow （ Fig. 2B ） . Interestingly, the PET-Spray showed some yellow circular spraying cues on the red background (Fig. 2B). And the diameters of these yellow patterns ranged from 1 µm to 160 µm, with 4% surface coverage. Therefore, we preliminarily infer two areas on PET-Spray: the yellow area is the BMP-2-TAMRA pattern area created by spray, the red area is the area of activated pattern without BMP-2-TAMRA, and its composition is similar to PET -Activated. The distribution of patterns from the ToF-SIMS image (Fig. 2B) is identical to the image obtained by our fluorescence microscopy (Fig. 2C).

According to the signal intensity labels in Figure 2B, yellow has stronger CN^- and CNO^- signals than red. The signals of CN^- and CNO^- represented by black are considered the background. Since it is difficult to avoid surface contamination, a small amount of CN^- and CNO^- were detected on the PET surface. Figure 2B allowed us to clearly and intuitively observe that all sample surfaces are homogenously modified. Next, as shown in Figure S2, the mass spectra were normalized by the peak at 49m/z (C_4H^-). We can evaluate CN^- and CNO^- signals by the ratio of CN^-/CH_4^- (the peak at 26 m/z /49 m/z) and CNO^-/CH_4^- (the peak at 42 m/z /49 m/z). Combined with Table 3 and Figure 2B, PET-BMP has the most CN^- and CNO^-(CN^-_{PET}: $CN^-_{PET\text{-}Activated}$: $CN^-_{PET\text{-}BMP}$: $CN^-_{PET\text{-}Spray\ with\ Activated\ pattern}$: $CN^-_{PET\text{-}Spray\ with\ BMP\text{-}2\text{-}TAMRA\ pattern}$ = 0.00: 0.53: 1.63: 0.33: 0.63; CNO^-_{PET}: $CNO^-_{PET\text{-}Activated}$: $CNO^-_{PET\text{-}BMP\text{-}2}$: $CNO^-_{PET\text{-}Spray1\ with\ Activated\ pattern}$: $CNO^-_{PET\text{-}Spray1\ with\ BMP\text{-}2\text{-}TAMRA\ pattern}$ = 0.10: 0.63: 1.92: 0.42: 0.73).

AFM

Figure 2d described the AFM height images after different modification steps. AFM images confirmed the overall homogeneous surface of the polymer before and after peptide grafting (Fig. 2D). Surface roughness after the different surface modification steps were presented in Table 4. According to the results obtained by scanning an area of 1 µm ×1 µm ((Fig. 2D (i)) and Table 4), surface functionalization with EDC/NHS did not show significant differences in the surface roughness of activated carboxyl-treated PET (RMS_{PET} = 1.6±0.6 nm, $RMS_{PET\text{-}Activated}$= 1.7±0.3 nm). Furthermore, after peptide grafting, it was noted that the surface topography did not change significantly, resulting in RMS surface roughness from 1.7 ± 0.3 nm on the PET-Activated surface to 1.2 ± 0.1 nm, 1.9 ± 0.6 nm, and 1.1 ± 0.1 nm after grafting of BMP-2-TAMRA, RGD-TAMRA, and a mixed solution of BMP-2-TAMRA and RGD-TAMRA, respectively. However, these differences were not statistically significant (at the level of $p \leq 0.05$).[9, 63, 70] We can conclude that we have a homogeneous grafting of peptides on PET surface whatever the peptide without aggregates.[71]

In addition, same conclusion was obtained by changing the scanning area. Figure 2d (ii) highlights the AFM images with a 20 µm ×20 µm scanning area which showing that the functionalized surface (PET, PET-Activated, and PET-Activated grafted with different peptides) were homogeneous with a similar roughness (Table 4).

Fluorescence Microscopy

TAMRA-coupled peptide density was quantified by fluorescence microscopy. No red fluorescence was observed on the PET surface before the grafting of fluorescent peptides (Fig. 2C). Moreover, the surface grafted with TAMRA-coupled peptide showed red fluorescence (Fig. 2C). The density of RGD-TAMRA peptide grafted onto PET was evaluated at 0.61±0.06 pmol/mm^2 and 0.84±0.05 pmol/mm^2 for PET-BMP-2-TAMRA. In the case of PET-Spray1, the density of BMP-2-TAMRA in the patterns (red patterning in Fig. 2C) was 0.81±0.1 pmol/mm^2. That means, we obtain similar BMP-2-TAMRA density whatever the grafting protocol used (Spray technology or in solution). In the case of PET-MIX1 and PET-MIX2, we quantified not only the whole density of peptides using RGD-TAMRA + BMP-2-TAMRA but also the density of each peptide using RGD-TAMRA + BMP-2 or RGD + BMP-2-TAMRA. On bifunctionalized surfaces, the surface density of RGD-TAMRA and BMP-2-TAMRA mimetic peptides was estimated at 0.68 ± 0.1 pmol/mm^2 and 0.03 ± 0.01 pmol/mm^2 for MIX1 and at 0.56 ± 0.05 pmol/mm^2 and 0.13 ± 0.03 pmol/mm^2 for MIX2, respectively.

The fluorescence images in Figure 2C demonstrate that the peptides were successfully grafted onto the PET surface and that these peptides were immobilized on the PET surface in a homogenous manner.

Immunocytochemical analysis

The use of immunocytochemistry staining permits the quantification of markers' expression and distributions and gives information about the cell shape and the percentage of cells with the same expression of markers. Here, we focused on five specific markers, RUNX2 (early osteoblast marker), OPN (late osteoblast marker), E11, DMP1 (early osteocyte marker) and SOST (later osteocyte marker), to evaluate the impact of ordered bioactive materials (with homogeneous RGD or/and BMP-2 peptides (PET-RGD, PET-BMP, PET-MIX1 and PET-MIX2)) and disordered bioactive materials (PET-Spray with cues of BMP-2 and RGD around). In addition, F-actin staining and DAPI were used to observe not only the cells' cytoskeleton and shape but also nuclei of cells seeded on different materials after 2 and 3 weeks of cell culture (Fig. 3).

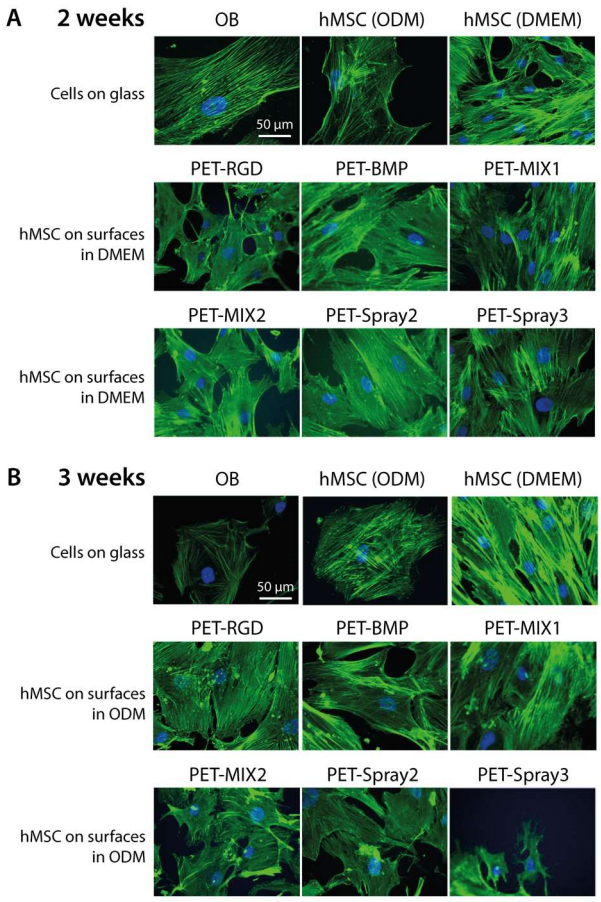

Figure 3. Fluorescence images of hMSC cultured for 2 weeks (A) and 3 weeks (B) on PET-RGD, PET-BMP, PET-Mix1, PET-Mix2, PET-Spray2 and PET-Spray3. The controls are: OB seeded on glass, hMSC on glass in normal medium and hMSC on glass in osteogenic medium. Cells were stained with conjugated phalloidin to detect F-actin and DAPI (nucleus). Objective 40x, scale bar is 50 µm.

Immunofluorescence assays were performed on cells to assess whether peptides and the distribution of the bioactive BMP-2 cues can impact on hMSC differentiation into osteogenic lineage. Osteoblast-seeded glass in osteoblast growth medium, hMSC-seeded glass in DMEM and ODM were used as controls.

To further investigate the effect of ordered and disordered bioactive cues on the osteogenic differentiation of hMSCs, hMSCs were seeded in DMEM medium for 2 weeks and in ODM medium for 2 and 3 weeks.

After 2 and 3 weeks, hMSCs cultured on glass in DMEM medium (Fig. 3A, B) proliferated rapidly, and the cells still exhibited a long and thin appearance. After 2 and 3 weeks, OBs are, as expected, cuboidal in shape and hMSC seeded on glass in ODM medium were cuboidal also in shape (Fig. 3A, B). On the other hand, after 2 weeks of culture, hMSCs cultured on the disordered BMP-2 cues (PET-Spray2 and PET-Spray3) formed columnar or cuboidal cells, which indicated that more osteoblasts were generated. After 3 weeks, Phalloidin staining shows that for PET-MIX2, PET-Spray 2 and PET-Spray3 lead to star-shaped cells with a dendritic morphology, which is typical of osteocytes (Fig. 3B).

Figure 5 demonstrated the aspect ratio (AR) variation across all surfaces after 2 and 3 weeks of culture. As shown in Figure 5A, after 2 weeks, the aspect ratios of PET-BMP, PET-MIX1, PET-MIX2, PET-Spray2 and PET-Spray3 were all close to 2.0, and there was no significant difference between groups. However, the aspect ratios of these five conditions were significantly different from the 2 control groups (hMSC on glass with and without ODM medium) and from the AR of PET-RGD. Interestingly, the AR of the condition “OB on glass” was significantly different from PET-RGD, PET-BMP, and PET-MIX1, but not significantly different from PET-MIX2, PET-Spray2 and PET-Spray3. It was mentioned that after 3 weeks’ culture, the AR of the control groups (hMSC on glass in DMEM) and PET-RGD significantly differed from PET-BMP, PET-MIX1, PET-Spray2 and PET-Spray3 (Fig. 5B, and S5). Interestingly, the AR of the condition “OB on glass” was not significantly different from these conditions. However, the AR of each condition after 2 weeks in DMEM medium was not significantly different from the AR of the same condition after 3 weeks in ODM medium (Fig. 5, S5).

Figure 5 showed the circularity results for all surfaces. After 2 weeks in DMEM medium, there was no significant difference among PET-BMP, PET-MIX1, PET-MIX2, PET-Spray2 and PET-Spray3 (Fig. 5A). All these conditions were not significantly different from hMSC on glass in ODM medium. The condition “OB on glass” was significantly different with hMSC on glass in DMEM medium, PET-RGD, PET-MIX1 and PET-Spray3 (Fig. 5A, S5). However, after 3 weeks’ culture in ODM medium (Fig 5B), PET-Spray3 had the lowest circularity value (0.26±0.20) and was significantly lower than PET-BMP and PET-MIX1. Furthermore, OB always showed stable and high circularity values, regardless of whether they were cultured for two weeks (0.56 ± 0.19) or three weeks (0.57 ± 0.19).

In addition, F-actin appeared crisscrossed, robust, and thicker and their parallel orientation gradually disappeared as hMSCs exhibited more pronounced osteoblast phenotypic markers. In fact, the lowest anisotropies of F-actin were observed when hMSC were seeded on glass in DMEM medium ($Anisority_{2W}$=0.45 ± 0.12; and $Anisority_{3W}$=0.44 ± 0.13) or on PET-RGD ($Anisority_{2W}$=0.36 ± 0.11; and $Anisority_{3W}$=0.37 ± 0.13) (Fig. 5). The highest anisotropy was obtained for PET-Spray3 whatever the time points for 2 weeks ($Anisority_{PET\text{-}Spray3}$=0.28 ± 0.10) and 3 weeks ($Anisority_{PET\text{-}Spray3}$=0.20 ± 0.09) respectively.

After 2 weeks, the RUNX2, OPN, E11, DMP1 and SOST nucleus's expressions of the condition “hMSCs on glass in DMEM medium” were very low (Fig. 4A, S4). Nevertheless, the OBs’ OPN expression in the nucleus was far superior to hMSC cultured on glass in DMEM and ODM medium (Fig. 4A, S4). The immunofluorescence results showed that cells seeded on PET grafted with both peptides (RGD + BMP-2) had a higher potential to induce osteogenic differentiation than the

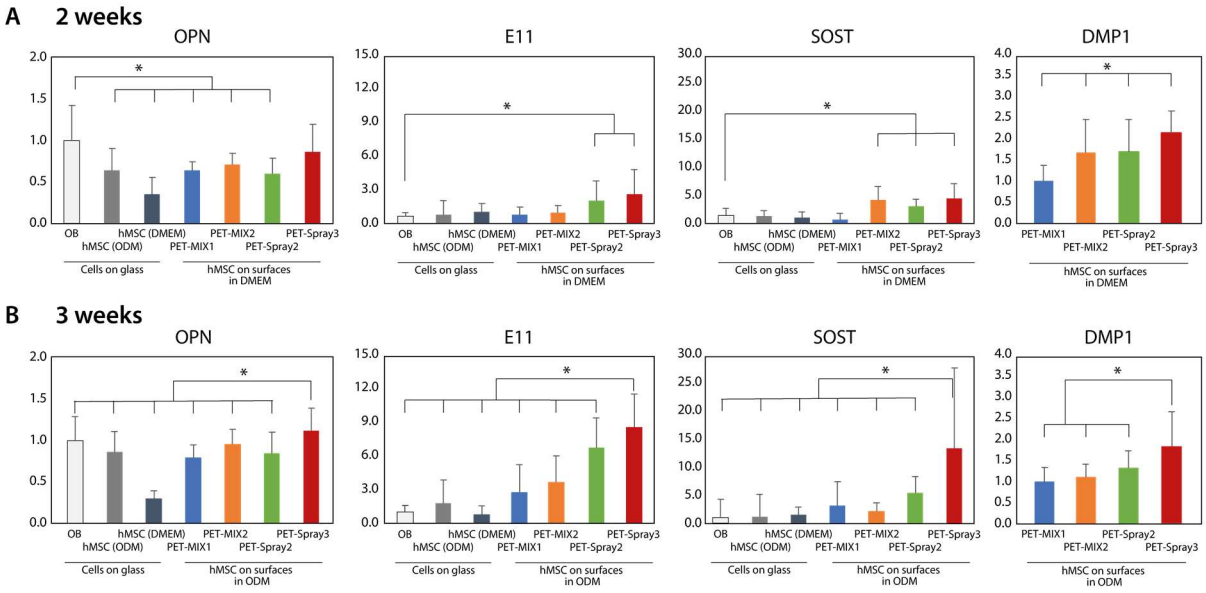

Figure 4. Quantitative analysis of the immunofluorescence of OPN, E11, SOST, and DMP1 after 2 weeks (A) and after 3 weeks (B) of culturing on PET-MIX1, PET-MIX2, PET-Spray2, PET-Spray3 in normal medium. Our controls: hMSC seeded on glass in normal and osteogenic medium and OB seeded on glass. The statistical analysis is presented on a supplementary data for clarity.

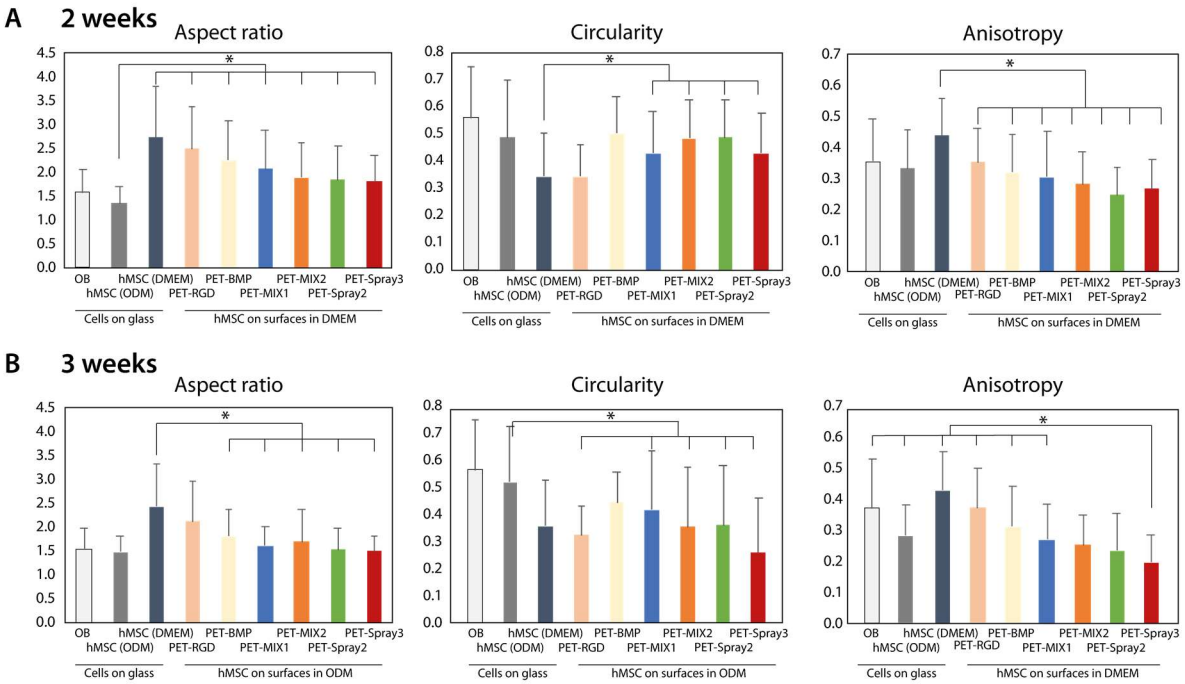

Figure 5. Quantitative analysis of the cell morphology culture on PET-RGD, PET-BMP, PET-MIX1, PET-MIX2, PET-Spray2, PET-Spray3. Aspect，circularity, and anisotropy after 2 weeks in normal medium (A), and after 3 weeks in osteogenic medium (B). Our controls: hMSC seeded on glass in normal and osteogenic medium and OB seeded on glass. The statistical analysis is presented on supplementary data for clarity.

single peptide without osteogenic differentiation medium (data not shown). Fluorescence images indicated that hMSC expressed RUNX2 marker on all conditions (PET-MIX1, PET-MIX2, PET-Spray2 and PET-Spray3) with no fluorescence intensity difference between them in DMEM and in ODM medium (data not shown). Our results highlighted an overexpression of OPN for all conditions in comparison with the control “hMSC seeded on glass in DMEM medium” (Fig. 3, S4). The 2 conditions with the highest overexpression of OPN were PET-Spray 3 and the control “OB on glass” (Fig. 3, S4). Our previous results highlighted an E11 overexpression in the case of PET-MIX2 and PET-MIX1 in comparison with PET-RGD and PET-BMP (data not shown) that’s why we selected PET-MIX1 and PET-MIX2 for our future experiments which have the same peptide density as PET-Spray2 and PET-Spray3 respectively to

assess the impact of the micro, nanodistribution of bioactive cues on hMSC differentiation. Fluorescence images revealed that PET-Spray2 and PET-Spray3 had an overexpression of E11 and DMP-1 after 2 weeks of culture in DMEM medium. Compared to all other conditions, PET-MIX2, PET-Spray2 and PET-Spray3 induced significantly higher expression of SOST. Immunostaining of osteogenic markers indicated that the surfaces with both peptides (homogeneous surfaces and PET-Spray) favored the osteogenic differentiation of hMSCs (Fig. 4).

Cell commitment into an osteoblastic lineage was also investigated after 2 (data not shown) and 3 weeks after seeding in osteogenic medium. The expression of RUNX2, OPN, E11, DMP1, and SOST was assessed. The control group was hMSCs on glass cultured in DMEM and ODM medium, and OBs cultured on glass.

All conditions overexpressed OPN compared with hMSC seeded on glass during 3 weeks in DMEM medium (Fig. 4, S4) which somewhat confirms the differentiation of hMSC into osteogenic lineage. A large number of hMSC maintained their stemness state on glass in DMEM medium. The OPN expression is higher in the case of PET-Spray3 (Fig. 4, S4). The fluorescence intensity of E11, DMP1 and SOST was similar for the 3 controls. The same tendency was observed for E11, DMP-1 and SOST for all the other conditions. A strong overexpression of the osteocyte markers was assessed in the case of PET-Spray2 and PET-Spray3. The ranking upon the expression of osteocyte markers could be: PET- Spray3>PET- Spray2>PET-MIX2>PET-MIX1>OB on glass> hMSC on glass in ODM medium. Surfaces with higher BMP whole density (PET-Spray3 and PET-MIX2) showed a higher osteocyte induction. Furthermore, PET with disordered cues of BMP-2 induced higher osteocyte commitment of hMSC in comparison with homogeneous MIX surfaces with the same density of peptides.

Discussion

In vivo, the cellular microenvironment has a crucial impact on regulating cell behaviors and functions. The most common method to induce the differentiation of MSCs is the treatment of the cell culture plates with medium containing multiple growth factors, proteins, and chemicals that have been proven to be highly effective in guiding MSC differentiation toward specific lineages. Specifically, osteogenic differentiation factors include bone morphogenetic protein (BMP), basic fibroblasts, dexamethasone, vitamin D3, beta glycerophosphate, and ascorbic acid have been reported to convert MSCs into osteoblasts with high efficacy.[72] But, cultured cells in Petri dishes and flasks receive completely different environmental cues compared to natural tissues, causing radical alterations in cell morphology and function.[73] While traditional materials/molecules, known as ‘soluble cues’ continue to show its effectiveness in MSC differentiation, other ‘insoluble cues’ have been reported to successfully regulate physical/mechanical properties of substrates in which cells attach, grow, and differentiate. Micropatterns, nanopatterns, nanoparticles and biohybrid materials have been widely used as physicochemical factors in conjunction with proper functionalities on material surfaces in order to (i) maintain multipotency of the MSCs for long-term culture,[74] (ii) control cell adhesion, migration and proliferation, and (iii) guide their differentiation into specific lineages.[9, 17-21, 23, 31, 36, 70, 74-77] Among various materials available for stem cell studies, carbon-based materials, including fullerenes, carbon nanotubes, and graphene/graphene oxide have shown potential for cell-friendly and cell adhesive materials with lower toxicity.[31, 76, 77] While both induction culture media and material mechanical properties have been reported to regulate the stem cell fate, little is known about which factor plays a more decisive role in directing the MSC differentiation lineage.[78] The underlying mechanisms for both regulating effects remain to be elucidated. Stem Cells (SC) reside in a niche made up of neighboring cells and the ECM infused with autocrine and paracrine soluble growth factors.[10] Cellular behavior depends on the abundance and distribution of bioactive factors in the ECM, which undergoes remodeling as a result of cells' self-renewal and differentiation.[12, 79] For instance, during MSCs proliferation, the native ECM has a higher concentration in fibroblast growth factor-2 (FGF-2),[80] while the ECM is richer in bone morphogenic protein-2 (BMP-2) during osteogenic differentiation. The interplay between SCs and these components seems rather intricate, and SC-ECM interactions are extensively studied.[14, 81] During the past decade, cell-material interactions have emerged as a leading research area in regenerative medicine.[14, 82, 83] Material scientists, including our group, [9, 17-21, 23, 31, 36, 37, 50, 71, 75, 77] have been designing a variety of biomimetic materials to reproduce cell-ECM interactions.[32, 84] Cellular behaviors are influenced by chemical cues, [9, 17-21, 23, 31, 36, 37, 50, 71, 75, 77] such as chemical composition, and ligand density,[85] as well as physical parameters such as matrix stiffness,[10, 20, 86-88] surface topography,[22, 26, 89, 90] and interfacial hydrophobicity of the microenvironment. Based on this knowledge,[91] many strategies to translate native ECM features to in vitro models use growth factors to control the fate of MSCs.[40, 92] BMPs induce the differentiation of mesenchymal cells towards chondrogenic and osteogenic lineages.[8, 93] The differentiation of hMSCs and progenitors towards the osteoblastic lineage is usually accomplished in response to BMP proteins or their mimetic peptides. BMPs interact with BMPR-I and BMPR-II receptors leading to the phosphorylation of BMPR-I by BMPR-II, which in turn activates Smad 1/5/8 signalling pathways.[94-96] This Smad-dependent pathway leads to an up-regulation of Runx-2 transcriptional factor, which in turn regulates the expression of other osteoblast-specific proteins such as bone sialoprotein (BSP) and osteopontin (OPN).[97] BMP-2 has been approved for clinical use by FDA in 2007.[92, 98] The most recognized adverse event related to BMP-2 use is ectopic bone formation, associated with BMP-2 leakage outside the implant site. An innovative approach consists in grafting biochemical cues onto the surface of bioinert materials to mimic physiological conditions. In fact, coatings made of adhesion proteins and growth factors have been used since a combination effect between growth factors

receptors and integrins were shown to regulate multiple biological events, including osteogenesis.[9, 17, 18, 20, 21, 31, 36, 50, 99]

In our work, PET was chosen as a model surface. Bioactive peptides able to favour not only MSC adhesion but also MSC differentiation into osteoblast lineage were grafted onto PET surface upon EDC/NHS activation. At each step of functionalization, TBO assay [36,100, 64, 67,68] and XPS were used to quantify the density of functional groups on the PET surface.

As shown in Fig. S1, there is a significant difference in the COOH density between native PET and PET-Activated. The density of COOH dropped from 30 pmol/mm^2 to 20 pmol/mm^2 after EDC/NHS activation. This result is consistent with other publications[36,64,67,68]. The activated carboxyl group on the surface of PET-Activated can chemically react with the amino group on the peptide, thereby grafting the peptide onto the surface of PET-Activated. Our results highlighted that the density of COOH was not significantly different between PET-Activated, PET-BMP, and PET-RGD. Considering each peptide contains two carboxylic groups (Fig. S1), one could expect to observe an increase of the density of COOH groups onto PET after peptide grafting. A certain decrease that has been however observed is likely connected with the effects of charged side chains of grafted peptides preventing the interaction of TBO^+ with the surface. [68]

We have also attempted to characterize the material at each functionalization stage by XPS. Basing on the previously published data, [36, 63] we have chosen nitrogen content (in atomic %), C/N (at. %/at.%) ratio and N-C=O content (mol. %) as characteristic values for functionalization monitoring. The nitrogen content values ($N_{PET-Activated}$: $N_{PET-BMP}$: $N_{PET-RGD}$= 1.7: 2.6: 1.0 at. %) was, as expected, slightly lower than those reported previously taking into account that no oxidation and hydrolysis were done on PET to increase the COOH density and then the peptide density [36] (2.8:3.1:2.1 at. %, respectively. As explained in Padiolleau's publication),[36] hydrolysis and oxidation of PET resulted in a higher COOH density on PET surface and then an increase of the hydrophilicity of virgin PET which was inconsistent with the spray technique. One of our objectives was to control the PET hydrophilicity before the spray process to avoid the coalescence of drops at liquid interfaces after spraying. However, using characteristic N−C=O band at 287.3 eV corresponding to peptide bonds, we could estimate the peptide content on the surface more precisely. The percentage of N-C=O is 1.1%, 2.2% and 0.7% in PET-Activated, PET-BMP and PET-RGD, respectively (Table 2). The increase of N-C=O content occurs due to the grafting of peptides on the surface (7 N-C=O groups per RGD peptide and 22 N-C=O groups per BMP peptide). However, the RGD and BMP-2 peptides likely have different accessibility to the surface due to the differences in size, that results in less efficient grafting of the latter.

Peptide densities were evaluated by fluorescence microscopy on PET solely or dually functionalized with fluorescent peptides. On PET containing only one peptide, the total peptide surface density was estimated to 0.61 ± 0.06 pmol/mm^2 and 0.84 ± 0.05 pmol/mm^2 on RGD-TAMRA and BMP-2-TAMRA PET surfaces, respectively. In Royer et al.,[63] the GRGDSK-TAMRA peptide density on the PET surface was evaluated at 1.9 ± 0.1 pmol/mm^2. Here, PET surfaces were firstly hydrolyzed and oxidized in order to create –COOH groups on PET surfaces.[63] As expected, our results showed lower peptide density immobilized onto PET surface without PET hydrolysis and oxidation to create more COOH groups. In previous work[38], the RGDC peptides densities obtained varied between 0.6 ± 0.04 pmol/mm^2 (using the same grafting conditions used in our work) and 1.7 ± 0.04 pmol/mm^2 (after hydrolysis and oxidation of PET). [85] Thus, our results are consistent with these results even though the evaluation of the density of peptides was performed with another technique (High resolution beta-imaging technique using radioelement). Kim et al. evaluated hMSCs osteogenic differentiation on modified tissue culture plastic (TCP) surfaces where the density of BMP-2 peptides was 0.69 pmol/ mm^2 .[63] In the same context, Moore et al. fabricated a linear gradient of BMP-2 peptide (0–1.4 pmol/mm^2) on glass surfaces and showed that at least 0.8 pmol/mm^2 is required to up-regulate Runx-2 gene expression.[63]

On the other hand, the dual peptide grafting; i.e. RGD + BMP-2 surfaces led to lower individual peptide densities as compared to the sole peptide grafting, which was expected. Indeed, on bifunctionalized surfaces, the surface density of RGD-TAMRA and BMP-2-TAMRA mimetic peptides was estimated at 0.68 ± 0.1 pmol/mm^2 and 0.03 ± 0.01 pmol/mm^2 for MIX 1 and at 0.56 ± 0.05 pmol/mm^2 and 0.13 ± 0.03 pmol/mm^2 for MIX 2, respectively. In other words, the global peptide density on bifunctionalized surfaces, estimated at 0.71 pmol/mm^2 for MIX1 and 0.69 pmol/mm^2 for MIX2 was close to that measured on surfaces containing only RGD-TAMRA or BMP-2-TAMRA (0.61 and 0.84 pmol/mm^2 respectively). These results are consistent with previous literature data showing that the grafting of pre-mixed RGD and BMP-2 peptides at equimolar concentration leads to a 50:50 combination, such that each peptide covers half of the whole surface.[101, 102,37,77]

To confirm the peptide grafting on geometrical cues, we used ToF-SIMS which is a very sensitive tool to characterize the micropatterns. We have selected two characteristic ions of nitrogen-containing functional groups (CN^-, CNO^-) for consideration (Fig. 2B). Being present in all samples of functionalized PET, these two ions served as functionalization markers, making it possible to probe the surface of materials. As it may be expected, distribution patterns of both ions are very similar in the same samples, with the relative intensity of signals increases as a function of surface modification (compare Fig. 2B). This result was further confirmed by XPS analysis (N-C=O%$_{PET}$=0.3%; N-C=O%$_{PET-Activated}$=1.1%; N-C=O%$_{PET-BMP}$=2.2%). Interestingly, using the same condition "PET-Spray1", we obtained similar distribution of the BMP patterns using ToF-SIMS and fluorescence microscopy: the size of the BMP-2-TAMRA pattern ranges from 1 μm to 160 μm (Fig. 2B, C).

Furthermore, many researchers pointed that the surface roughness played an important role in directing cell differentiation.[36] AFM was used to evaluate the roughness of materials at each step of the functionalization. Interestingly, PET-Spray has similar surface topography and roughness ($R_{PET\text{-}Spray}$ = 1.2 ± 0.2 nm) with PET-BMP, although PET-Spray was prepared using the Spray technique to create disordered BMP-2-TAMRA micropatterns on PET-Activated. As concluded previously with fluorescence microscopy results, AFM results confirmed that all the peptides were grafted homogeneously onto PET.

The grafted RGD onto surfaces favors cell adhesion. It was known that very few hMSC adhere on virgin PET surfaces[38]. After peptide grafting, using a sole (RGD or BMP-2) or a dual peptide grafting (RGD+ BMP (MIX1 or MIX2) or PET-Spray), hMSC adhere on PET surfaces. Interestingly, the higher overexpression of OPN was observed when hMSCs were seeded on PET with both peptides (Fig. 4). The literature has recently demonstrated that homogeneously co-conjugated RGD/BMP-2 peptides onto PET surfaces significantly enhanced hMSCs osteogenesis as compared to the solely homogeneous grafting of BMP-2 or RGD peptides. Biological results showed that the osteogenic commitment of hMSCs was enhanced on bifunctionalized surfaces as compared to surfaces containing BMP-2, while on RGD surfaces cells mainly preserved their stemness character. [9, 36, 63] Several parameters need to be taken into consideration, including the length of the linker between the carboxyl groups and cell-binding peptides moieties to ensure high accessibility of the peptide functional groups to the cell-surface receptors. [19-21, 35,36,103, 104]

Interesting findings have been reported regarding the specification of hMSCs into specialized phenotypes in response to microscale spatially distributed ligands. For example, Bilem et al.[17,18] provide clear evidence that hMSCs perceive geometric cues in their microenvironment, it is quite intriguing that RGD/BMP-2 micropatterns shaped as triangles and squares significantly enhanced hMSCs osteogenesis, while those shaped as rectangles exerted no specific effect on hMSCs fate, as compared to homogeneous surfaces. One possible explanation is that triangular and square micropatterns elicit more drastic changes in cytoskeleton organization as compared to rectangular geometries. Padiolleau et al.[37] demonstrated that the combinations of peptides with RGD and BMP-2 mimetic peptides could further induce stem cell differentiation when appropriately organized on the surface. The patterning must be relatively small (area less than 625 μm^2) and sharp in terms of their shapes (such as rectangles). Among all the concentrations assessed, a 50/50 combination of RGD and BMP-2 appears to be the best mixture to promote osteogenic differentiation. McBeath et al. cultured MSCs on different microsized fibronectin islands (1024, 2025, and 10 000 μm^2) for 1 week in mixed osteogenic/adipogenic media. They found that MSCs seeded on the largest micro islands differentiate preferentially toward osteoblast phenotype, whereas those on relatively small microislands tend to differentiate into adipocytes. All these publications used photolithography technique to elaborate bioactive micropatterns of different geometries on the surface. It should be noted that the originality of our work is to elaborate disordered bioactive patterns on polymer surfaces using a low-cost technique.

Meanwhile, Matthew et al. used EBL technology to fabricate nanotopography with different symmetries and degrees of disorder on the PMMA surface. They studied the interaction of osteoprogenitor cells and mesenchymal stem cells with these materials' surfaces. Their results first presented that disordered topography may be an effective strategy for inducing differentiation: highly ordered nano topologies have negligible effects on cell adhesion and osteoblast differentiation, whereas with random nanocues cells exhibited a more osteoblastic morphology after 14 days.[60, 63, 102, 105] Previous studies have found that ordered nanopits can reduce cell adhesion. Moreover, disordered nanopits can better promote the osteogenic differentiation of embryonic stem cells .[106] Our results are in good agreement with this study: PET- Spray3 (with highly disordered bioactive patterns (drops with a large difference in diameter and a large difference in spacings between drops)) showed significantly higher OPN expression than PET-MIX2 (with ordered and homogeneous topography). In the same way, PET-Spray2 showed significantly higher OPN expression than PET-MIX1 (same density of peptides for both conditions). To sum up, not only the bioactivity of the surface (that means the selected peptides) but also the distribution of peptides' micropatterns impact on hMSC fate. More precisely, using DMEM or ODM medium, disordered bioactive BMP-2 cues revealed a higher expression of osteocyte markers (early (E11 and DMP-1) or late markers (SOST)) than PET functionalized with not only RGD but also BMP-2 peptides (with the same densities of each peptide in the 2 conditions) (Fig. 4A, B).

This result convinced that a few cells on PET-Spray 3 already exhibited mature osteocyte characteristics, while most of cells still maintained the characteristics of pre-osteocytes or later osteoblasts.

As an hMSC attached and spread on a surface, the morphology of the hMSC shifted from elongated spindle-shaped MSCs to a range of potential morphologies, such as: cuboidal or polygonal-shaped MSCs or MSCs demonstrating multiple large processes, referred to as stellate morphologies. Morphological results showed that hMSC morphology generally tended to have an elongated and flattened shape, characterized by high anisotropy, high aspect ratio, and low circularity.[107, 108] Most of the induced cells grown to be cuboidal in shape, showing low anisotropy, low aspect ratio, and high circularity.[109, 110] Few cells were induced to tend to stellate morphology, exhibiting low anisotropy, low aspect ratio, and moderate circularity.[111-113]

We examined temporal changes in aspect ratio, circularity and actin anisotropy to assess the MSC morphology changes in response

to all PET surfaces functionalized with bioactive peptides homogeneously or with micro/nanopatterns. A quantitative assessment of cell morphology, summarized in Figure 5, confirmed these observations after 2 and 3 weeks of cell culture. After 2 weeks, hMSCs cultured in DMEM medium on glass had the highest anisotropy (0.45), most significant aspect ratio (2.73) and lowest circularity (0.34) (Fig. 5, S5). Gultian et al. found that the MSC had approximately an aspect ratio from 2.5 to 5 and a circularity from 0.4 to 0.7 depending on the stiffness of the materials.2 OB on glass showed lower anisotropy (0.37), lower aspect ratio (1.58) and highest circularity (0.56) (Fig. 5).[17, 114] The AR of PET-BMP, PET-MIX1, PET-MIX2, PET-Spray2, and PET-Spray3 were 2.26 ± 0.81, 2.07 ± 0.83, 1.89 ± 0.75, 1.85 ± 0.70, 1.81 ± 0.56; and their circularity were 0.50 ± 0.14, 0.43 ± 0.16, 0.48 ± 0.14, 0.49 ± 0.14, 0.43 ± 0.15. These osteoblast values were consistent with the data of Rabel et al.: the aspect ratio was 2, the circularity was 0.6.[115] This indicated that after 2 weeks' culture in DMEM medium, hMSCs on PET-BMP, PET-MIX1, PET-MIX2, PET-Spray2, and PET-Spray3 were induced to osteoblast, and their cell morphology was similar to OB. In contrast, more changes were observed after 3 weeks' culture in differentiation medium. Previous studies have shown that MSC exhibit increased actin anisotropy when they undergo osteogenic differentiation.[116] It is worth mentioning that hMSC on PET-Spray3 in differentiation medium had the lowest anisotropy value (0.20) and the lowest circularity value (0.26). Verbruggen et al. observed the circularity of osteocyte to be 0.23. In contrast, OB had higher anisotropy (0.37), lower aspect ratio (1.52) and highest circularity (0.57). These results showed that PET-Spray3 had lower anisotropy and circularity than OB, which means PET-Spray3 has a more disordered F-actin and an increasingly elongated shape trend.

The clinical translation of mesenchymal stem cells (MSCs) is limited by population heterogeneity and inconsistent responses to engineered signals. Our objective is the fabrication of an innovative coating (a smart cell culture plate) for the rapid production at high yields of osteoblast cells from hMSC of a patient. To the best of our knowledge, our study represents the first in vitro differentiation of hMSCs into osteocytes using 2D disordered micropatterned surfaces, which therefore constitutes a major step forward for the study of hMSCs osteogenic differentiation and osteocyte function in bone, and for bone reconstruction. Moreover, this is the first time that a spray technology was used to synthesize disordered bioactive micro, nano patterned surfaces for the study of their impact on MSC differentiation. Most of the studies with a focus on disordered cues on surfaces are interested in topographical cues.[90] Taken together, even though further investigations are required to fully elucidate these finding, these results obtained not only with immunocytochemistry but also cell shape analyses suggest that the combination of chemical and geometric cues was able to direct stem cell fate. Our results showed that culture and induction of hMSCs with conventional culture medium and conventional osteogenic medium resulted in a same conclusion: disordered bioactive micro, nano patterned PET surfaces with the highest density of BMP-2 was the best candidate.

The spraying protocol described in the present work is easily adaptable to large-scale manufacturing, enabling control of the stem cell onto various 2D or 3D disordered bioactive micro, nanopatterns onto polymer surface. Traditional electron-beam lithography (EBL) nano, microfabrication was limited to patterning on planar substrates and often involves various chemicals in lithographic steps. Compared with EBL technology, it is easy with spray technique to obtain at low-cost patterns of bioactive molecules.[90] We argue that the stacking of individually patterned 2D materials using spray technology could enable 3D printing at atomic resolution, even though this has not been demonstrated here .[117]

Materials and Methods

Materials

PET samples were taken from a commercial crystalline biaxially oriented film obtained from Goodfellow. The bioriented film had a thickness of 0.1 mm. Dimethylaminopropyl-3-ethylcarbodiimideethylcarbodiimide hydrochloride (EDC), N-hydroxysuccinimide (NHS), and 2-(N-morpholino)-ethanesulfonic acid (MES) were purchased from Sigma-Aldrich (France). Native and TAMRA-labelled peptides KGRGDSPC, K(TAMRA)-GRGDSPC (RGD), and KIPKASSVPTELSAISMLYLK, KIPKASSVPTELSAISMLYLK(TAMRA) (BMP-2) peptides were synthesized by GeneCust (Boynes, France). Bone marrow mesenchymal stem cells (hMSCs), human osteoblasts (OB), Mesenchymal stem cell growth medium 2, SupplementMix MSC growth medium 2, MSC osteogenic differentiation medium, SupplementMix MSC osteogenic diff. medium and osteoblast growth medium, and Supplement Mix osteoblast growth medium were purchased from PromoCell GmbH (Heidelberg, Germany). Dulbecco's modified eagle Medium (D-MEM), Dulbecco's phosphate buffered saline (1X) (PBS), Trypsin-EDTA, Fetal bovine serum (FBS), Alexa Fluoroshield™ 488 Phalloidin, Secondary antibodies (Goat anti-Mouse IgG (H+L) Highly Cross-Adsorbed Secondary Antibody Alexa Fluoroshield™ 647 and Goat anti-Rabbit IgG (H+L) Highly Cross-Adsorbed Secondary Antibody Alexa Fluoroshield™ 647), and DAPI were obtained from Thermo Fisher Scientific (USA). Primary antibody against RUNX2 Rabbit mAb was acquired from Cell Signaling (USA). Mouse anti-osteopontin (OPN) was bought from Santa Cruz Biotechnology (USA). Mouse monoclonal anti-podoplanin (E11) antibody and Rabbit polyclonal anti-Sclerostin (SOST) were purchased from Abcam (EL ROZENBURG, Germany). DMP1 monoclonal antibody (DMP1) was purchased from Abnova (Taiwan, China) Tween 20, Triton X-100, Bovine serum albumin (BSA), and Trypan Blue solution were obtained from Sigma (USA). Antibiotic/Antimycotic solution were obtained from GE Healthcare Life Sciences (USA).

Surface conjugation with mimetic peptides

PET was ultrasonically cleaned with ethanol for 1 h and immersed in a solution of EDC (0.2M), NHS (0.1M) and MES (0.1M) in MilliQ water at room temperature for 1 h to convert the surface's carboxylic acid groups into activated esters.

We used EDC/NHS/MES to activate the carboxyl groups on the PET surface (Figure 1). Since this cross-linking reaction must be performed in a buffer devoid of extraneous carboxyls and amine groups, we chose to use MES buffer (4-morpholinoethanesulfonic acid). The EDC/NHS coupling protocol was used to improve efficiency and generate dry, stable intermediates containing activated ester groups. The resulting materials were called "PET-Activated". All peptides were first dissolved in DMSO. The activated surface was immersed into the RGD-TAMRA, BMP-2-TAMRA or mixed RGD and BMP-2 solution (10 µM with MilliQ water) for 16 h at room temperature. After covalent immobilization, the surfaces were sonicated 6 times with Milli-Q water for 15 min to remove the physically attached peptides. The resulting materials were called "PET-RGD", "PET-BMP", "PET-MIX1" (3% BMP-2+97% RGD), "PET-MIX2" (23% BMP-2+77% RGD).

Due to the primary amines and carboxylic acids in peptides, the activated carboxyl groups on the surface of the activated material are easy to link to the primary amines in the polypeptide. The steps of surface modification PET, PET-Activated, PET-BMP, and PET-RGD were shown in Figure 1.

An automatic spray gun (PILOT WA 450, WALTHER Spritz- und Lackiersysteme GmbH, Germany) was mounted on a rail. Air cap (0.3-1.8mm, V1136030050*) was connected to the spray gun. A pressure regulator (BD-26-8-6) was used to control air pressure. A syringe pump (R99-EB, Razel Scientific Instruments) was plugged between the spray gun and a 20 cc/mL Terumo syringe without needle (Terumo Europe N.V.). A controlled table (PROLABO) enables a maximum displacement of 10 cm to adjust the distance between the nozzle and the material. To prepare bioactive micro, nanopatterned PET (called "PET-Spray"), we used a Spray technology. A homemade prototype was fabricated.

BMP-2-TAMRA peptide was sprayed at a concentration of 10 µM in 7.5% glycerol solution, which can control the viscosity to ensure that the patterned biomolecules were sufficiently grafted onto the material surface. The volume and flow of liquid were controlled by a micropump. The distribution of micropatterning can be controlled by adjusting the distance between the spray nozzle and material, the liquid flow speed, the spray time, and the air pressure. The PET-Spray surfaces were kept at 4°C for 4 days to obtain the higher peptide density onto PET surface. Then, the surfaces were sonicated 6 times with Milli-Q water for 15 min to remove the physically attached peptides.

For ToF-SIMS and AFM characterizations, the air pressure, flow speed, and spray time values were 0.5 bar, 50 µl/min and 3 s, respectively, to obtain drops from 3 to 152 µm in diameter and a value of 3% for BMP-2-TAMRA surface coverage. For cell experiments, we designed 4 spray conditions: PET-Spray1 (using the setup values of 0.5 bar, 50 µl/min, 3 s), PET-Spray2 (with 0.5 bar, 200 µl/min, 1 s), PET-Spray3 (1 bar, 200 µl/min, 3 s), and PET-Spray4 (2 bar, 150 µl/min, 1 s). As shown in Table 1, PET-Spray1 and PET-Spray4 have similar BMP-2 peptide surface coverage but different peptide distribution. For example, PET-Spray1 has approximately 86.9%, 7.5 % and 3.7 % of drops between 0-10 µm, 10-20 µm and 20-30 µm, respectively. In contrast, PET-Spray2 and PET-Spray3 have different BMP-2 peptide surface coverage, but their distribution is similar. The PET-Spray materials had 2 different areas: patterns grafted with BMP-2-TAMRA peptide, the rest of the surface is functionalized with EDC/NHS.

Toluidine Blue Assay

A toluidine blue O (TBO) assay was performed on the surfaces to quantify the density of carboxylic acid groups on the PET surface after the different modification steps. Basically, square PET samples (1 cm × 1 cm) were immersed in 10 mL of TBO/ NaOH solution (0.5 mM, pH = 10) for 6 h under stirring in the dark at room temperature. The main aim of this step was to obtain interactions between TBO molecules (positively charged) and COO^- groups on the surface of PET. Then, the PET surfaces were washed once with 10 mL of NaOH solution (pH 10) and twice with 10 mL of MilliQ water. The samples were then immersed in 5 mL of 50% acetic acid for 10 minutes to facilitate the release of the adsorbed complex dyes (TBO molecules) from the sample surface.[100] Finally, the wash solutions from the different samples were transferred to wells of a 96-well culture plate (200 µL/well), and the spectrometer measured the absorbance at 633 nm. Based on the assumption that 1 mol of TBO^+ molecule is complexed with 1 mol of surface COO^- groups, the concentration of carboxyl groups can be determined from the calibration curve.[63, 118] To construct a calibration curve, we prepared TBO solutions ranging from 0.1 to 0.00001 mM by dissolving TBO powder in 50% acetic acid solution and measured their absorbance

at 630 nm using a spectrophotometer (Biotek, ELx808 absorbance reader). The recorded absorbance was then translated to the carboxyl groups' density according to the calibration curve (Fig. S1).[119] The carboxyl groups were quantified in triplicate for each surface modification condition. Furthermore, the sample's surface carboxyl group concentration (pmol/mm^2) was calculated according to the surface area.

X-ray Photoelectron Spectroscopy (XPS)

Table 1. Parameters used for spray technique and the obtained distribution of spots (% for each diameter)

	Air pressure (bar)	Speed (µl/min)	Time (s)	0-10 µm	10-20µm	20-30µm	30-40µm	40-50µm	50+ µm	Average diameter	Surface coverage
PET-Spray1	0.5	50	3	86.9	7.5	3.7	0	0.9	0.9	9.2	2.9
PET-Spray2	0.5	200	1	54.4	23.5	8.8	1.5	4.4	7.4	16	4.5
PET-Spray3	1	200	3	52.1	26.7	6.8	0.7	2.7	11	20.6	23.3
PET-Spray4	2	150	1	51.5	28.7	14.9	4.0	1.0	0	13.2	3.2

Table 2. XPS analyses of PET surfaces at each step of peptide grafting

	C (%)	O (%)	N (%)	C/N (%)	C/O (%)	C-C (%)	C-CO (%)	C-O (%)	N-C=O (%)	COOR (%)
PET	72.3	27.7	0.1	\	2.6	30.3	13.0	14.4	0.3	12.5
PET-Activated	71.8	26.5	1.7	42.2	2.7	30.4	11.5	16.2	1.1	12.4
PET-BMP	71.5	25.8	2.6	27.5	2.8	32.2	9.5	15.8	2.2	11.3
PET-RGD	72.4	26.6	1.0	72.4	2.7	30.1	14.3	14.2	0.7	12.1

After each step of the peptide grafting, surface chemical compositions were determined by XPS using a Thermo Fisher Scientific K-ALPHA spectrometer. No fluorescent peptides were used for XPS analysis. PET materials were analyzed with a monochromatized Al-Kα source (hν = 1486.6 eV) and a 400 µm X-Ray spot size. Five measurements per sample were carried out to ascertain the reproducibility of the surface chemistry. The survey spectra (0-1100 eV) were recorded by using a constant pass energy of 200 eV, while high-resolution spectra were recorded with a continuous pass energy of 40 eV. Charge neutralization was applied during the analysis. High-resolution spectra (i.e., C1s, O1s, N1s) shifted versus the main C1s component at around 284.8 eV were quantified using the Avantage software provided by Thermo Fisher Scientific. The main attention was paid to the C1s and N1s spectra by fitting to discuss the chemical bonding. Three replicates per condition were tested and five measurements per sample were carried out to ascertain the homogeneity of the surface modification.

Time-of-Flight Secondary Ion Mass Spectrometry (ToF-SIMS)

ToF-SIMS analyses were performed using a ToF-SIMS (ION-TOF) instrument located at PLACAMAT (University of Bordeaux). We used an electron flood gun to compensate for charges on samples. To obtain high mass resolution spectra for these samples, we took a pulsed $Bi3^+$ primary ion beam at 30 keV, and the current at 0.30 pA. The spatial resolution of the image acquired under this setting is 128 x 128 pixels for a scanning area of 500 x 500µm. It means the pixel size is around 4 µm. This size corresponds to the primary beam size we used. For the mass resolution, the CN^- peak width was around 1.7 ns that corresponds to 0.007 m/z. For the references, we made 150 scans.

Atomic Force Microscopy (AFM)

AFM was used to characterize the roughness and morphology (Dimension Fast scan AFM, Bruker). FastScan-C probes (40 µm long silicon nitride cantilevers with pyramidal silicon tips of 5 nm tip radius; resonance frequency : 300 kHz; nominal spring constant : 0.8 N/m) were used in tapping mode to characterize the sample surface in air at room temperature. To better evaluate the surface roughness and morphology of the samples, we set two different image sizes of AFM scanning area: 20 µm× 20 µm and 1 µm × 1 µm. Figure 2d showed the AFM height image obtained by 1 µm × 1 µm (Fig. 2D(i)), and 20 µm × 20 µm (Fig. 2D(ii)), respectively. The root-mean-square surface roughness (R) was calculated via Nanoscope analysis software. Three independent measurements were performed on each sample to ascertain the homogeneity of the surface modification.

Evaluation of Peptide Density by Fluorescence Microscopy

The density of peptides immobilized onto PET surfaces was evaluated by fluorescence microscopy (using a Leica DM5500B microscope, Germany). To do so, fluorescent peptides (peptides linked to fluorescent dyes through lysine (K)) were grafted onto PET, according to our protocol described above and our previous papers.[9,36, 63, 85] To quantify covalently grafted peptides, PET surfaces were functionalized with RGD-TAMRA, BMP-2-TAMRA, BMP-2-TAMRA and RGD-TAMRA, BMP-2 and RGD-TAMRA, BMP-2-TAMRA and RGD. After the grafting of fluorescent peptides onto PET and after the washing step, images were taken at 2.5x Objective. The parameters set were: Bin1, Gain2 and 1000 ms for the exposure time. The same parameters were applied to all images. Each sample was in triplicate, and 10 different areas per sample were analyzed. The fluorescence intensity of peptide-TAMRA grafted onto the PET surface was quantified by Image J software. The surface density of each fluorescent peptide grafted was measured using the calibration curve in pmol/mm^2 (Fig. S3 a, b). To do so, a series of droplets of RGD-TAMRA and BMP-2-TAMRA peptides with known concentrations (from 10 nM to 10 µM) were deposited on virgin PET surfaces. These

Table 3. Mass spectra normalized by the peak at 49m/z (C4H-)

	PET	PET-Activated	PET-BMP	PET-Spray1 with Activated pattern	PET-Spray1 with BMP-2-TAMRA pattern
CN^-/C_4H^-	0	0.53	1.63	0.33	0.63
$CNO^-/C4H^-$	0.10	0.63	1.92	0.42	0.73

Table 4. Surface roughness after the different surface modification steps

	Scanned Area	PET	PET-Activated	PET-BMP	PET-RGD	PET-MIX1	PET-Spray1
Roughness (RMS)(nm)	1 x 1 μm^2	1.6±0.6	1.7±0.3	1.2±0.1	1.9±0.6	1.1±0.1	1.2±0.2
	20 x 20 μm^2	1.8±0.5	1.7±0.8	1.8±1.3	1.4±0.2	1.5±0.5	4.0±3.9

peptide droplets were then imaged at the same Objective and exposure time, and a standard curve was constructed for each peptide. Then, the fluorescence intensity on different peptide-modified surfaces was quantified by

Leica MMAF software, and the peptide density was evaluated according to the standard curve in pmol/mm^2.

Cell Culture

hMSCs were thawed and cultured in mesenchymal stem cell growth medium in a humidified environment containing 5% (vol/vol) CO_2 at 37 °C. Subsequently, cells were subcultured using 0.25% Trypsin/EDTA 1x detachment. hMSCs were seeded on sterilized material in DMEM medium without serum at a density of 750 cells/cm^2 and 3000 cells/cm^2 for cell differentiation experiments in DMEM medium or in osteogenic differentiation medium, respectively. All the materials were sterilized with 70% Ethanol overnight. After 6 hours of incubation, the culture medium was replaced with supplemented 10% (vol/vol) FBS and DMEM. After 24 hours, the culture medium was replaced with 10% FBS, DMEM medium and 1% antibiotic solution in cell experiments without osteogenic differentiation medium, and hMSC osteogenic differentiation medium supplemented with 1% antibiotic solution in cell experiments with osteogenic differentiation medium. The nomenclature used to identify the culture medium is: “ODM” for osteogenic differentiation medium and “DMEM” for DMEM medium. Cells were then cultured for 2 or 3 weeks, and all the media were replaced every 72 hours. Human osteoblasts (OB) were thawed and cultured in osteoblast growth medium. Then OB were seeded on sterilized glass slides at a density of 20,000 cells/cm^2 in osteoblast growth medium and changed twice a week. Finally, the cells were fixed with 4% paraformaldehyde (PFA) at 24 h, 1 week, 2 weeks and 3 weeks, and kept in PBS solution at 4℃ for immunofluorescence assays.

Immunofluorescence Staining

All samples were permeabilizated with 0.5 % Triton/PBS for 15 min at 4 ºC and saturated with 1% BSA/PBS for 30 min at 37 ºC. Afterwards, cells were incubated with various primary antibodies diluted in 1% BSA/PBS for 1h in a humidified chamber at 37 ºC: RUNX2 monoclonal antibody (Rabbit) at 1/1600 dilution, OPN monoclonal antibody (Mouse) at 1 µg/mL concentration, E11 monoclonal antibody (Mouse) antibody at 2 µg/mL concentration, SOST monoclonal antibody (Rabbit) at 5 µg/mL concentration, and DMP1 monoclonal antibody (Mouse) at 10 µg/mL concentration. After washing samples with 0.05 % Tween 20 / PBS, cells were incubated with the secondary antibody at a concentration of 5 µg/mL in 1% BSA/PBS for 1h in a humidified chamber at 37 ºC: Goat anti-Mouse IgG (H+L) Highly Cross-Adsorbed Secondary Antibody Alexa Fluoroshield™ 647 and Goat anti-Rabbit IgG (H+L) Highly Cross-Adsorbed Secondary Antibody Alexa Fluoroshield™ 647. Subsequently, cells were incubated in Alexa Fluoroshield™ 488 Phalloidin at a dilution of 1/40 for 1h at 37 ºC to describe cell morphology and cytoskeleton organization. Finally, cells were stained for nuclei by DAPI at 1/1000 dilution for 1h in the dark and at 4°C. Fluorescently stained samples were observed by an epifluorescence microscope (Leica DM5500B) and taken by Metamorph software (10x and 40x Objective). Image files were opened with Image J (freely available from: www.nih.gov) and converted to 16-bit files. These fluorescence images were then used to determine the intensity of the red colour emitted by the label from which was subtracted the background signal measured on hMSCs cultures on PET or glass surfaces and only incubated with the secondary antibody Alexa Fluor 647. Fluorescence intensity measurements were performed on at least 40-60 cells per each type

of surface.

Cell Shape

After 2 and 3 weeks of culture, cytoskeletons and nuclei of cells were fluorescently stained, with F-actins labelled by Phalloidin and nuclei by DAPI. Aspect ratios (ARs), circularities and anisotropy were measured by outlining cells in fluorescence images with ImageJ. AR was defined as the ratio of the particle's fitted ellipse, Major Axis /Minor Axis, which were obtained from the two eigenvalues of the corresponding cell profile calculated by the ImageJ software. Circularity is quantified by area multiplied by 4π divided by the square of the perimeter. A value of 1.0 indicated a perfect circle. As the value approaches 0.0, it indicated an increasingly elongated shape. The orientation of F-actin in cells (anisotropy) was quantified using an ImageJ plug-in "FibrilTool", according to Boudaoud et al.[120] protocol. Briefly, raw images taken under fluorescence microscopy at 40× Objective were opened with ImageJ. A region of interest (ROI) was drawn using the tool to select one cell. Then, FibrilTool plug-in was used to measure the degree of F-actin orientation by means of anisotropy parameter that varies from 0 to 1. 0 corresponds to disordered F-actin (purely isotropic fibers), and 1 means that F-actin fibers are perfectly ordered (parallel fibers). The measurements were made on 40-60 individual cells per condition.

Statistical Analysis

Data are means ± SD of at least three independent trials. Significant differences between treatment means were assessed by one-way ANOVA in Origin (Origin Lab, Northampton, MA, USA). Significant differences were determined for p values of at least ≤0.05. * p ≤0 .05, ** p ≤0 .01, and *** p ≤0 .001.

Conclusions

Here, we reported a rationally designed bioinspired coating with intrinsic biochemical cues that provides a suitable environment for bone regeneration. This work provides a robust strategy for directing mesenchymal stem cells differentiation into an osteogenic lineage, which can be utilized as a potential cell culture platform to understand cell–substrate or cell–cell interactions, further developing tissue repair and stem cell-based therapies.

We aimed to offer a new insight on how the distribution of bioactive micro, nanopatterns on a surface can influence the regulation of stem cell differentiation. hMSCs were seeded on bioactive polymers homogeneously functionalized with RGD or/and BMP-2 peptides and on disordered bioactive materials with micro, nanopatterns of BMP-2 mimetic peptides. Our results showed that a bioactive homogeneous grafting co-conjugated with RGD and BMP-2 peptides leads to higher osteoblast differentiation than a single peptide grafting. Seeding hMSCs on surfaces co-conjugated with higher BMP-2 content resulted in inducing osteogenic differentiation effectively. hMSCs seeded on surfaces with random bioactive nano, micropatterns exhibited more pronounced osteoblastic morphology after 14 days in DMEM medium without osteogenic factors. This finding opens further therapeutic avenues for development of research platforms and medical devices. Importantly, we showed that disordered bioactive micro, nanopatterns significantly increased the osteocyte differentiation upon culturing in the osteogenic differentiation medium for 21 days. The enhanced differentiation suggests that the disordered topography fabricated by spray could be an effective strategy to direct the hMSCs fate for bone regenerative medicine and tissue engineering. Our immediate perspectives involve performing qPCR analyses to study osteogenic differentiation genes and assessing mineral deposition using Alizarin Red and von Kossa stainings.

Author Contributions

Yujie Zhang: Conceptualization, Validation, Formal Analysis, Investigation, Writing – Original Draft, Visualization. Murielle Rémy: Methodology, Review. Evgeny Apartsin: Writing, Review. Emilie Prouvé: Methodology. Cécile Feuillie: AFM Methodology, Investigation, Review. Christine Labrugère: XPS Methodology, XPS writing. Nithavong Cam: Tof-SIMS Methodology, Tof-SIMS writing. Marie-Christine Durrieu: Conceptualization, Validation, Writing & Editing, Supervision, Funding Acquisition.

Conflicts of interest

The authors declare that they have no known competing financial interests or personal relationships that could have appeared to influence the work reported in this paper.

Acknowledgements

The authors thank Professor Gaetan Laroche from Laval University for his help for the design of the spray technique and Christel Chanseau for her help for chemical experiments. This work was supported by the French "Agence Nationale de la Recherche" (ANR-21-CE06-0031-02) (M.C.D.). Y.Z. acknowledges financial support from China Scholarship Council.

References

1. Arthur, A.; Gronthos, S., Clinical Application of Bone Marrow Mesenchymal Stem/Stromal Cells to Repair Skeletal Tissue. *International Journal of Molecular Sciences* **2020,** DOI: 10.3390/ijms21249759.

2. Undale, A. H.; Westendorf, J. J.; Yaszemski, M. J.; Khosla, S., Mesenchymal Stem Cells for Bone Repair and Metabolic Bone Diseases. *Mayo Clin Proc* **2009,** *84* (10), 893-902.

3. Stamnitz, S.; Klimczak, A., Mesenchymal Stem Cells, Bioactive Factors, and Scaffolds in Bone Repair: From Research Perspectives to Clinical Practice. *Cells* **2021,** DOI: 10.3390/cells10081925.

4. Campana, V.; Milano, G.; Pagano, E.; Barba, M.; Cicione, C.; Salonna, G.; Lattanzi, W.; Logroscino, G., Bone substitutes in orthopaedic surgery: from basic science to clinical practice. *Journal of Materials Science: Materials in Medicine* **2014,** *25* (10), 2445-2461.

5. Deng, L.; Yan, Y., Research status and progress of biomaterials for bone repair and reconstruction. *Zhongguo Xiu Fu Chong Jian Wai Ke Za Zhi* **2018,** *32* (7), 815-820.
6. Wang, S.; Xu, P.; Li, X.; Su, X.; Chen, Y.; Wan, L.; Fan, L.; Yin, K.; Liu, Y.; Zhao, C. R., Mesenchymal Stem Cells and Cell Therapy for Bone Repair. *Current Molecular Pharmacology* **2016,** *9* (4), 289-299.
7. Andrzejewska, A.; Lukomska, B.; Janowski, M., Concise Review: Mesenchymal Stem Cells: From Roots to Boost. *Stem Cells* **2019,** *37* (7), 855-864.
8. Yi, M.-H.; Lee, J.-E.; Kim, C.-B.; Lee, K.-W.; Lee, K.-H., Locally Controlled Diffusive Release of Bone Morphogenetic Protein-2 Using Micropatterned Gelatin Methacrylate Hydrogel Carriers. *BioChip Journal* **2020,** *14* (4), 405-420.
9. Bilem, I.; Chevallier, P.; Plawinski, L.; Sone, E. D.; Durrieu, M. C.; Laroche, G., RGD and BMP-2 mimetic peptide crosstalk enhances osteogenic commitment of human bone marrow stem cells. *Acta Biomaterialia* **2016,** *36*, 132-142.
10. Discher, D. E.; Mooney, D. J.; Zandstra, P. W., Growth factors, matrices, and forces combine and control stem cells. *Science* **2009,** *324* (5935), 1673-1677.
11. James, A. W., Review of Signaling Pathways Governing MSC Osteogenic and Adipogenic Differentiation. *Scientifica* **2013,** DOI: 10.1155/2013/684736.
12. Keung, A. J.; Kumar, S.; Schaffer, D. V., Presentation counts: microenvironmental regulation of stem cells by biophysical and material cues. *Annu Rev Cell Dev Biol* **2010,** *26*, 533-556.
13. Doyle, S. M.; Genest, O.; Wickner, S., Protein rescue from aggregates by powerful molecular chaperone machines. *Nature Reviews Molecular Cell Biology* **2013,** *14* (10), 617-629.
14. Walters, N. J.; Gentleman, E., Evolving insights in cell–matrix interactions: Elucidating how non-soluble properties of the extracellular niche direct stem cell fate. *Acta Biomaterialia* **2015,** *11*, 3-16.
15. Xue, N.; Ding, X.; Huang, R.; Jiang, R.; Huang, H.; Pan, X.; Min, W.; Chen, J.; Duan, J.-A.; Liu, P., Bone tissue engineering in the treatment of bone defects. *Pharmaceuticals* **2022,** DOI: 10.3390/ph15070879.
16. Quarto, R.; Giannoni, P., Bone tissue engineering: past–present–future. *Mesenchymal Stem Cells: Methods and Protocols* **2016**, 21-33.
17. Bilem, I.; Chevallier, P.; Plawinski, L.; Sone, E. D.; Durrieu, M.-C.; Laroche, G., Interplay of Geometric Cues and RGD/BMP-2 Crosstalk in Directing Stem Cell Fate. *ACS Biomaterials Science & Engineering* **2017,** *3* (10), 2514-2523.
18. Bilem, I.; Plawinski, L.; Chevallier, P.; Ayela, C.; Sone, E. D.; Laroche, G.; Durrieu, M. C., The spatial patterning of RGD and BMP-2 mimetic peptides at the subcellular scale modulates human mesenchymal stem cells osteogenesis. *Journal of Biomedical Materials Research Part A* **2018,** *106* (4), 959-970.
19. Zouani, O. F.; Chollet, C.; Guillotin, B.; Durrieu, M.-C., Differentiation of pre-osteoblast cells on poly(ethylene terephthalate) grafted with RGD and/or BMPs mimetic peptides. *Biomaterials* **2010,** *31* (32), 8245-8253.
20. Zouani, O. F.; Rami, L.; Lei, Y.; Durrieu, M.-C., Insights into the osteoblast precursor differentiation towards mature osteoblasts induced by continuous BMP-2 signaling. *Biology Open* **2013,** *2* (9), 872-881.
21. Zouani, O. F.; Kalisky, J.; Ibarboure, E.; Durrieu, M.-C., Effect of BMP-2 from matrices of different stiffnesses for the modulation of stem cell fate. *Biomaterials* **2013,** *34* (9), 2157-2166.
22. Das, R. K.; Zouani, O. F.; Labrugère, C.; Oda, R.; Durrieu, M.-C., Influence of nanohelical shape and periodicity on stem cell fate. *ACS nano* **2013,** *7* (4), 3351-3361.
23. Cheng, Z. A.; Zouani, O. F.; Glinel, K.; Jonas, A. M.; Durrieu, M.-C., Bioactive chemical nanopatterns impact human mesenchymal stem cell fate. *Nano letters* **2013,** *13* (8), 3923-3929.
24. M.C. Durrieu, Z. O. Zouani, FR Pat., M.C. Durrieu, Z. O. Zouani, FR Pat., 1352302, 2014; PT Pat, BR112015020439A2, 2019; EU Pat, EP2968660A1, 2019; KR Pat, KR20150126669A, 2019; CN Pat, CN105073150A, 2019; US Pat, US2016022875A1, 2019.
25. Huang, Y.-S.; Bertrand, V.; Bozukova, D.; Pagnoulle, C.; Labrugère, C.; De Pauw, E.; De Pauw-Gillet, M.-C.; Durrieu, M.-C., RGD surface functionalization of the hydrophilic acrylic intraocular lens material to control posterior capsular opacification. *PloS one* **2014,** DOI: 10.1371/journal.pone.0114973.
26. Cunha, A.; Zouani, O. F.; Plawinski, L.; Botelho do Rego, A. M.; Almeida, A.; Vilar, R.; Durrieu, M.-C., Human mesenchymal stem cell behavior on femtosecond laser-textured Ti-6Al-4V surfaces. *Nanomedicine* **2015,** *10* (5), 725-739.
27. Lei, Y.; Zouani, O. F.; Remy, M.; Ayela, C.; Durrieu, M.-C., Geometrical Microfeature Cues for Directing Tubulogenesis of Endothelial Cells. *PLoS ONE* **2012,** DOI: 10.1371/journal.pone.0041163.
28. Li, Y.; Zhao, C.; Luo, F.; Liu, Z.; Gui, X.; Luo, Z.; Zhang, X.; Li, D.; Liu, C.; Li, X., Amyloid fibril structure of α-synuclein determined by cryo-electron microscopy. *Cell Research* **2018,** *28* (9), 897-903.
29. Lei, Y.; Zouani, O. F.; Rami, L.; Chanseau, C.; Durrieu, M.-C., Modulation of Lumen Formation by Microgeometrical Bioactive Cues and Migration Mode of Actin Machinery. *Small* **2013,** *9* (7), 1086-1095.
30. Zouani, O. F.; Chanseau, C.; Brouillaud, B.; Bareille, R.; Deliane, F.; Foulc, M.-P.; Mehdi, A.; Durrieu, M.-C., Altered nanofeature size dictates stem cell differentiation. *Journal of Cell Science* **2012,** *125* (5), 1217-1224.
31. Zouani, O. F.; Lei, Y.; Durrieu, M.-C., Pericytes, stem-cell-like cells, but not mesenchymal stem cells are recruited to support microvascular tube stabilization. *Small (Weinheim an der Bergstrasse, Germany)* **2013,** *9* (18), 3070-3075.
32. Murphy, W. L.; McDevitt, T. C.; Engler, A. J., Materials as stem cell regulators. *Nat Mater* **2014,** *13* (6), 547-57.
33. Yao, X.; Hu, Y.; Cao, B.; Peng, R.; Ding, J., Effects of surface molecular chirality on adhesion and differentiation of stem cells. *Biomaterials* **2013,** *34* (36), 9001-9009.
34. Benoit, D. S. W.; Schwartz, M. P.; Durney, A. R.; Anseth, K. S., Small functional groups for controlled differentiation of hydrogel-encapsulated human mesenchymal stem cells. *Nature Materials* **2008,** *7* (10), 816-823.
35. Padiolleau, L.; Chanseau, C.; Durrieu, S.; Ayela, C.; Laroche, G.; Durrieu, M. C., Directing hMSCs fate through geometrical cues and mimetics peptides. *Journal of biomedical materials research. Part A* **2020,** *108* (2), 201-211.
36. Padiolleau, L.; Chanseau, C.; Durrieu, S.; Chevallier, P.; Laroche, G.; Durrieu, M.-C., Single or Mixed Tethered Peptides To Promote hMSC Differentiation toward Osteoblastic Lineage. *ACS Applied Bio Materials* **2018,** *1* (6), 1800-1809.
37. Huang, Y. S.; Bertrand, V.; Bozukova, D.; Pagnoulle, C.; Labrugère, C.; De Pauw, E.; De Pauw-Gillet, M. C.; Durrieu, M. C., RGD surface functionalization of the hydrophilic acrylic intraocular lens material to control posterior capsular opacification. *PLoS One* **2014,** DOI: 10.1371/journal.pone.0114973.
38. Chollet, C.; Chanseau, C.; Remy, M.; Guignandon, A.; Bareille, R.; Labrugere, C.; Bordenave, L.; Durrieu, M. C., The effect of RGD density on osteoblast and endothelial cell behavior on RGD-grafted polyethylene terephthalate surfaces. *Biomaterials* **2009,** *30* (5), 711-20.

39. Akhmanova, M.; Osidak, E.; Domogatsky, S.; Rodin, S.; Domogatskaya, A., Physical, spatial, and molecular aspects of extracellular matrix of in vivo niches and artificial scaffolds relevant to stem cells research. *Stem cells international* **2015,** DOI: 10.1155/2015/167025.
40. Lutolf, M. P.; Blau, H. M., Artificial Stem Cell Niches. *Advanced Materials* **2009,** *21* (32-33), 3255-3268.
41. Andolfi, A.; Arnaldi, P.; Di Lisa, D.; Pepe, S.; Frega, M.; Fassio, A.; Lagazzo, A.; Martinoia, S.; Pastorino, L., A micropatterned thermoplasmonic substrate for neuromodulation of in vitro neuronal networks. *Acta Biomaterialia* **2023,** *158*, 281-291.
42. Phuah, E. W. C.; Hart, W. L.; Sumer, H.; Stoddart, P. R., Patterning of biomaterials by aerosol jet printing: A parametric study. *Bioprinting* **2020,** DOI: 10.1016/j.bprint.2020.e00081.
43. Humenik, M.; Winkler, A.; Scheibel, T., Patterning of protein-based materials. *Biopolymers* **2021,** DOI: 10.1002/bip.23412.
44. Shin, H., Fabrication methods of an engineered microenvironment for analysis of cell–biomaterial interactions. *Biomaterials* **2007,** *28* (2), 126-133.
45. Ilkhanizadeh, S.; Teixeira, A. I.; Hermanson, O., Inkjet printing of macromolecules on hydrogels to steer neural stem cell differentiation. *Biomaterials* **2007,** *28* (27), 3936-3943.
46. Zhang, Z.; Yoo, R.; Wells, M.; Beebe, T. P.; Biran, R.; Tresco, P., Neurite outgrowth on well-characterized surfaces: preparation and characterization of chemically and spatially controlled fibronectin and RGD substrates with good bioactivity. *Biomaterials* **2005,** *26* (1), 47-61.
47. Deng, W.; Zhang, X.; Wang, L.; Wang, J.; Shang, Q.; Zhang, X.; Huang, L.; Jie, J., Wafer-Scale Precise Patterning of Organic Single-Crystal Nanowire Arrays via a Photolithography-Assisted Spin-Coating Method. *Advanced Materials* **2015,** *27* (45), 7305-7312.
48. Muneekaew, S.; Wang, M.-J.; Chen, S.-y., Control of stem cell differentiation by using extrinsic photobiomodulation in conjunction with cell adhesion pattern. *Scientific Reports* **2022,** DOI: 10.1038/s41598-022-05888-3.
49. Lee, C.-Y.; Hu, S.-M.; Christy, J.; Chou, F.-Y.; Ramli, T. C.; Chen, H.-Y., Biointerface Coatings With Structural and Biochemical Properties Modifications of Biomaterials. *Advanced Materials Interfaces* **2023,** DOI: 10.1002/admi.202202286.
50. Padiolleau, L.; Chanseau, C.; Durrieu, S.; Ayela, C.; Laroche, G.; Durrieu, M.-C., Directing hMSCs fate through geometrical cues and mimetics peptides. *Journal of Biomedical Materials Research Part A* **2020,** *108* (2), 201-211.
51. Liu, W.; Zhou, Z.; Zhang, S.; Shi, Z.; Tabarini, J.; Lee, W.; Zhang, Y.; Gilbert Corder, S. N.; Li, X.; Dong, F.; Cheng, L.; Liu, M.; Kaplan, D. L.; Omenetto, F. G.; Zhang, G.; Mao, Y.; Tao, T. H., Precise Protein Photolithography (P3): High Performance Biopatterning Using Silk Fibroin Light Chain as the Resist. *Advanced Science* **2017,** DOI: 10.1002/advs.201700191.
52. O'Hagan, M. P.; Duan, Z.; Huang, F.; Laps, S.; Dong, J.; Xia, F.; Willner, I., Photocleavable Ortho-Nitrobenzyl-Protected DNA Architectures and Their Applications. *Chemical Reviews* **2023,** *123* (10), 6839-6887.
53. Paik, S.; Kim, G.; Chang, S.; Lee, S.; Jin, D.; Jeong, K.-Y.; Lee, I. S.; Lee, J.; Moon, H.; Lee, J., Near-field sub-diffraction photolithography with an elastomeric photomask. *Nature communications* **2020,** DOI: 10.1038/s41467-020-14439-1.
54. Eichinger, C. D.; Hsiao, T. W.; Hlady, V., Multiprotein microcontact printing with micrometer resolution. *Langmuir* **2012,** *28* (4), 2238-2243.
55. Watson, J. L.; Aich, S.; Oller-Salvia, B.; Drabek, A. A.; Blacklow, S. C.; Chin, J.; Derivery, E., High-efficacy subcellular micropatterning of proteins using fibrinogen anchors. *J Cell Biol* **2021,** DOI: 10.1083/jcb.202009063.
56. Wang, X.; Li, S.; Yan, C.; Liu, P.; Ding, J., Fabrication of RGD Micro/Nanopattern and Corresponding Study of Stem Cell Differentiation. *Nano Letters* **2015,** *15* (3), 1457-1467.
57. Dalby, M. J.; Gadegaard, N.; Tare, R.; Andar, A.; Riehle, M. O.; Herzyk, P.; Wilkinson, C. D. W.; Oreffo, R. O. C., The control of human mesenchymal cell differentiation using nanoscale symmetry and disorder. *Nature Materials* **2007,** *6* (12), 997-1003.
58. Lou, J.; Mooney, D. J., Chemical strategies to engineer hydrogels for cell culture. *Nature Reviews Chemistry* **2022,** *6* (10), 726-744.
59. Hu, Y.; Yao, X.; Liu, Q.; Wang, Y.; Liu, R.; Cui, S.; Ding, J., Left-Right Symmetry or Asymmetry of Cells on Stripe-Like Micropatterned Material Surfaces. *Chinese Journal of Chemistry* **2018,** *36* (7), 605-611.
60. Gagne, L.; Laroche, G., Engineering Biomaterials Surfaces Using Micropatterning. *Advanced Materials Research* **2007,** *15-17*, 77-82.
61. Lionetto, F.; Lionetto, M. G.; Mele, C.; Corcione, C. E.; Bagheri, S.; Udayan, G.; Maffezzoli, A., Autofluorescence of model polyethylene terephthalate nanoplastics for cell interaction studies. *Nanomaterials* **2022,** DOI: 10.3390/nano12091560.
62. Van de Voorde, B.; Benmeridja, L.; Giol, E. D.; Van der Meeren, L.; Van Damme, L.; Liu, Z.; Toncheva, A.; Raquez, J.-M.; Van den Brande, N.; Skirtach, A., Potential of poly (alkylene terephthalate) s to control endothelial cell adhesion and viability. *Materials Science and Engineering: C* **2021,** DOI: 10.1016/j.msec.2021.112378.
63. Royer, C.; Guay-Bégin, A.-A.; Chanseau, C.; Chevallier, P.; Bordenave, L.; Laroche, G.; Durrieu, M.-C., Bioactive micropatterning of biomaterials for induction of endothelial progenitor cell differentiation: Acceleration of in situ endothelialization. *Journal of Biomedical Materials Research Part A* **2020,** *108* (7), 1479-1492.
64. Fang, D.; He, F.; Xie, J.; Xue, L., Calibration of Binding Energy Positions with C1s for XPS Results. *Journal of Wuhan University of Technology-Mater. Sci. Ed.* **2020,** *35* (4), 711-718.
65. Delaittre, G.; Goldmann, A. S.; Mueller, J. O.; Barner-Kowollik, C., Efficient Photochemical Approaches for Spatially Resolved Surface Functionalization. *Angewandte Chemie International Edition* **2015,** *54* (39), 11388-11403.
66. Massonnet, P.; Heeren, R. M. A., A concise tutorial review of TOF-SIMS based molecular and cellular imaging. *Journal of Analytical Atomic Spectrometry* **2019,** *34* (11), 2217-2228.
67. Zhou, C.; Sun, D.; Garcia, R.; Stevie, F. A., Determination of chemical composition in multilayer polymer film using ToF-SIMS. *Analytical Methods* **2018,** *10* (21), 2444-2449.
68. Wu, G.; Paz, M. D.; Chiussi, S.; Serra, J.; González, P.; Wang, Y. J.; Leon, B., Excimer laser chemical ammonia patterning on PET film. *Journal of Materials Science: Materials in Medicine* **2008,** *20* (2), DOI: 10.1007/s10856-008-3600-5.
69. Yahia, L. H.; Mireles, L. K., X-ray photoelectron spectroscopy (XPS) and time-of-flight secondary ion mass spectrometry (ToF SIMS). **2017**, 83-97.
70. Nishida, K.; Baba, K.; Murakami, D.; Tanaka, M., Nanoscopic analyses of cell-adhesive protein adsorption on poly(2-methoxyethyl acrylate) surfaces. *Biomaterials Science* **2022,** *10* (11), 2953-2963.
71. Lei, Y.; Rémy, M.; Labrugère, C.; Durrieu, M.-C., Peptide immobilization on polyethylene terephthalate surfaces to study specific endothelial cell adhesion, spreading and migration. *Journal of Materials Science: Materials in Medicine* **2012,** *23* (11), 2761-2772.
72. Tatavarty, R.; Ding, H.; Lu, G.; Taylor, R. J.; Bi, X., Synergistic acceleration in the osteogenesis of human mesenchymal stem cells by graphene oxide–calcium phosphate nanocomposites. *Chemical Communications* **2014,** *50* (62), 8484-8487.

73. Loncaric, D.; Labat, V.; Debeissat, C.; Brunet de la Grange, P.; Rodriguez, L.; Vlaski-Lafarge, M.; Ivanovic, Z., The majority of cells in so-called "mesenchymal stem cell" population are neither stem cells nor progenitors. *Transfusion Clinique et Biologique* **2019,** *26* (4), 316-323.
74. Stevens, M. M.; George, J. H., Exploring and engineering the cell surface interface. *Science* **2005,** *310* (5751), 1135-1138.
75. Gaharwar, A. K.; Avery, R. K.; Assmann, A.; Paul, A.; McKinley, G. H.; Khademhosseini, A.; Olsen, B. D., Shear-Thinning Nanocomposite Hydrogels for the Treatment of Hemorrhage. *ACS Nano* **2014,** *8* (10), 9833-9842.
76. Putra, V. D.; Kilian, K. A.; Knothe Tate, M. L., Biomechanical, biophysical and biochemical modulators of cytoskeletal remodelling and emergent stem cell lineage commitment. *Communications Biology* **2023,** DOI: 10.1038/s42003-022-04320-w.
77. Royer, C.; Bégin, A.-A. G.; Plawinski, L.; Lévesque, L.; Durrieu, M.-C.; Laroche, G., Validation of reference genes for real-time PCR of cord blood mononuclear cells, differentiating endothelial progenitor cells, and mature endothelial cells. *Experimental Cell Research* **2018,** *370* (2), 389-398.
78. Zhu, M.; Li, W.; Dong, X.; Yuan, X.; Midgley, A. C.; Chang, H.; Wang, Y.; Wang, H.; Wang, K.; Ma, P. X.; Wang, H.; Kong, D., In vivo engineered extracellular matrix scaffolds with instructive niches for oriented tissue regeneration. *Nature Communications* **2019,** *10* (1), DOI: 10.1038/s41467-019-12545-3.
79. Tang, R.-Z.; Liu, X.-Q., Biophysical cues of in vitro biomaterials-based artificial extracellular matrix guide cancer cell plasticity. *Materials Today Bio* **2023**, DOI: 10.1016/j.mtbio.2023.100607.
80. Tsutsumi, S.; Shimazu, A.; Miyazaki, K.; Pan, H.; Koike, C.; Yoshida, E.; Takagishi, K.; Kato, Y., Retention of Multilineage Differentiation Potential of Mesenchymal Cells during Proliferation in Response to FGF. *Biochemical and Biophysical Research Communications* **2001,** *288* (2), 413-419.
81. Watt, F. M.; Huck, W. T. S., Role of the extracellular matrix in regulating stem cell fate. *Nature Reviews Molecular Cell Biology* **2013,** *14* (8), 467-473.
82. Lee, J.; Abdeen, A. A.; Zhang, D.; Kilian, K. A., Directing stem cell fate on hydrogel substrates by controlling cell geometry, matrix mechanics and adhesion ligand composition. *Biomaterials* **2013,** *34* (33), 8140-8148.
83. Yao, X.; Peng, R.; Ding, J., Cell–Material Interactions Revealed Via Material Techniques of Surface Patterning. *Advanced Materials* **2013,** *25* (37), 5257-5286.
84. Kanchanawong, P.; Calderwood, D. A., Organization, dynamics and mechanoregulation of integrin-mediated cell–ECM adhesions. *Nature Reviews Molecular Cell Biology* **2023,** *24* (2), 142-161.
85. Chollet, C.; Chanseau, C.; Remy, M.; Guignandon, A.; Bareille, R.; Labrugère, C.; Bordenave, L.; Durrieu, M.-C., The effect of RGD density on osteoblast and endothelial cell behavior on RGD-grafted polyethylene terephthalate surfaces. *Biomaterials* **2009,** *30* (5), 711-720.
86. Fu, J.; Wang, Y.-K.; Yang, M. T.; Desai, R. A.; Yu, X.; Liu, Z.; Chen, C. S., Mechanical regulation of cell function with geometrically modulated elastomeric substrates. *Nature methods* **2010,** *7* (9), 733-736.
87. Prouvé, E.; Rémy, M.; Feuillie, C.; Molinari, M.; Chevallier, P.; Drouin, B.; Laroche, G.; Durrieu, M.-C., Interplay of matrix stiffness and stress relaxation in directing osteogenic differentiation of mesenchymal stem cells. *Biomaterials Science* **2022,** *10* (17), 4978-4996.
88. Prouvé, E.; Drouin, B.; Chevallier, P.; Rémy, M.; Durrieu, M.-C.; Laroche, G., Evaluating Poly(Acrylamide-co-Acrylic Acid) Hydrogels Stress Relaxation to Direct the Osteogenic Differentiation of Mesenchymal Stem Cells. *Macromolecular Bioscience* **2021,** DOI: 10.1002/mabi.202100069.
89. Pedrosa, C. R.; Arl, D.; Grysan, P.; Khan, I.; Durrieu, S.; Krishnamoorthy, S.; Durrieu, M.-C., Controlled Nanoscale Topographies for Osteogenic Differentiation of Mesenchymal Stem Cells. *ACS Applied Materials & Interfaces* **2019,** *11* (9), 8858-8866.
90. Dalby, M. J.; Gadegaard, N.; Tare, R.; Andar, A.; Riehle, M. O.; Herzyk, P.; Wilkinson, C. D.; Oreffo, R. O., The control of human mesenchymal cell differentiation using nanoscale symmetry and disorder. *Nature materials* **2007,** *6* (12), 997-1003.
91. Ayala, R.; Zhang, C.; Yang, D.; Hwang, Y.; Aung, A.; Shroff, S. S.; Arce, F. T.; Lal, R.; Arya, G.; Varghese, S., Engineering the cell–material interface for controlling stem cell adhesion, migration, and differentiation. *Biomaterials* **2011,** *32* (15), 3700-3711.
92. Fernandez de Grado, G.; Keller, L.; Idoux-Gillet, Y.; Wagner, Q.; Musset, A.-M.; Benkirane-Jessel, N.; Bornert, F.; Offner, D., Bone substitutes: a review of their characteristics, clinical use, and perspectives for large bone defects management. *Journal of Tissue Engineering* **2018,** DOI: 10.1177/2041731418776819.
93. Cerri, D. G.; Rodrigues, L. C.; Alves, V. M.; Machado, J.; Bastos, V. A. F.; Carmo Kettelhut, I. d.; Alberici, L. C.; Costa, M. C. R.; Stowell, S. R.; Cummings, R. D., Endogenous galectin-3 is required for skeletal muscle repair. *Glycobiology* **2021,** *31* (10), 1295-1307.
94. Aluganti Narasimhulu, C.; Singla, D. K., The role of bone morphogenetic protein 7 (BMP-7) in inflammation in heart diseases. *Cells* **2020,** DOI: 10.3390/cells9020280.
95. Bragdon, B.; Thinakaran, S.; Moseychuk, O.; King, D.; Young, K.; Litchfield, D. W.; Petersen, N. O.; Nohe, A., Casein kinase 2 β-subunit is a regulator of bone morphogenetic protein 2 signaling. *Biophysical journal* **2010,** *99* (3), 897-904.
96. Firdauzy, M. A. B.; Setiawatie, E. M.; Roestamadji, R. I.; Haque, N., Collagen in Bovine Dentine Promotes BMP2 and Osterix Expression In Bone Healing. *Malaysian Journal of Medicine and Health Sciences* **2023,** *19*, 194-197.
97. Kim, J.; Pan, H., Effects of magnesium alloy corrosion on biological response – Perspectives of metal-cell interaction. P*rogress in Materials Science* **2023,** DOI: 10.1016/j.pmatsci.2022.101039.
98. Krishnakumar, G. S.; Roffi, A.; Reale, D.; Kon, E.; Filardo, G., Clinical application of bone morphogenetic proteins for bone healing: a systematic review. *International Orthopaedics* **2017,** *41* (6), 1073-1083.
99. Park, J. S.; Yang, H. N.; Jeon, S. Y.; Woo, D. G.; Na, K.; Park, K.-H., Osteogenic differentiation of human mesenchymal stem cells using RGD-modified BMP-2 coated microspheres. *Biomaterials* **2010,** *31* (24), 6239-6248.
100. Huong, D. T. M.; Chai, W. S.; Show, P. L.; Lin, Y.-L.; Chiu, C.-Y.; Tsai, S.-L.; Chang, Y.-K., Removal of cationic dye waste by nanofiber membrane immobilized with waste proteins. *International Journal of Biological Macromolecules* **2020,** *164*, 3873-3884.
101. Moore, N. M.; Lin, N. J.; Gallant, N. D.; Becker, M. L., Synergistic enhancement of human bone marrow stromal cell proliferation and osteogenic differentiation on BMP-2-derived and RGD peptide concentration gradients. *Acta Biomaterialia* **2011,** *7* (5), 2091-2100.
102. Kim, Y.; Renner, J. N.; Liu, J. C., Incorporating the BMP-2 peptide in genetically-engineered biomaterials accelerates osteogenic differentiation. *Biomaterials Science* **2014,** *2* (8), 1110-1119.
103. Jia, J.; Coyle, R. C.; Richards, D. J.; Berry, C. L.; Barrs, R. W.; Biggs, J.; Chou, C. J.; Trusk, T. C.; Mei, Y., Development of peptide-

functionalized synthetic hydrogel microarrays for stem cell and tissue engineering applications. *Acta biomaterialia* **2016,** *45*, 110-120.
104. Sung, T.-C.; Wang, T.; Liu, Q.; Ling, Q.-D.; Subbiah, S. K.; Renuka, R. R.; Hsu, S.-T.; Umezawa, A.; Higuchi, A., Cell-binding peptides on the material surface guide stem cell fate of adhesion, proliferation and differentiation. *Journal of Materials Chemistry B* **2023,** 11, 1389-1415.
105. Gagné, L.; Rivera, G.; Laroche, G., Micropatterning with aerosols: application for biomaterials. *Biomaterials* **2006,** *27* (31), 5430-5439.
106. Xing, F.; Li, L.; Zhou, C.; Long, C.; Wu, L.; Lei, H.; Kong, Q.; Fan, Y.; Xiang, Z.; Zhang, X., Regulation and Directing Stem Cell Fate by Tissue Engineering Functional Microenvironments: Scaffold Physical and Chemical Cues. *Stem Cells International* **2019,** DOI: 10.1155/2019/2180925.
107. Kim, C.; Young, J. L.; Holle, A. W.; Jeong, K.; Major, L. G.; Jeong, J. H.; Aman, Z. M.; Han, D.-W.; Hwang, Y.; Spatz, J. P.; Choi, Y. S., Stem Cell Mechanosensation on Gelatin Methacryloyl (GelMA) Stiffness Gradient Hydrogels. *Annals of Biomedical Engineering* **2020,** *48* (2), 893-902.
108. Gultian, K. A.; Gandhi, R.; Sarin, K.; Sladkova-Faure, M.; Zimmer, M.; de Peppo, G. M.; Vega, S. L., Human induced mesenchymal stem cells display increased sensitivity to matrix stiffness. *Scientific Reports* **2022,** DOI: 10.1038/s41598-022-12143-2.
109. Uslu, E.; Mimiroglu, D.; Ercan, B., Nanofeature Size and Morphology of Tantalum Oxide Surfaces Control Osteoblast Functions. *ACS Applied Bio Materials* **2021,** *4* (1), 780-794.
110. Perez-Moreno, A.; Reyes-Peces, M. d. l. V.; de Los Santos, D. M.; Pinaglia-Tobaruela, G.; de la Orden, E.; Vilches-Pérez, J. I.; Salido, M.; Piñero, M.; de la Rosa-Fox, N., Hydroxyl groups induce bioactivity in silica/chitosan aerogels designed for bone tissue engineering. In vitro model for the assessment of osteoblasts behavior. *Polymers* **2020,** DOI: 10.3390/polym12122802.
111. Rabel, K.; Kohal, R.-J.; Steinberg, T.; Tomakidi, P.; Rolauffs, B.; Adolfsson, E.; Palmero, P.; Fürderer, T.; Altmann, B., Controlling osteoblast morphology and proliferation via surface micro-topographies of implant biomaterials. *Scientific Reports* **2020,** DOI: 10.1038/s41598-020-69685-6.
112. Long, E. G.; Buluk, M.; Gallagher, M. B.; Schneider, J. M.; Brown, J. L., Human mesenchymal stem cell morphology, migration, and differentiation on micro and nano-textured titanium. *Bioact Mater* **2019,** *4*, 249-255.
113. Yao, S.; Du, Z.; Xiao, L.; Yan, F.; Ivanovski, S.; Xiao, Y., Morphometric Changes of Osteocyte Lacunar in Diabetic Pig Mandibular Cancellous Bone. *Biomolecules* **2023,** DOI: 10.3390/biom13010049.
114. Gautam, S.; Sharma, C.; Purohit, S. D.; Singh, H.; Dinda, A. K.; Potdar, P. D.; Chou, C. F.; Mishra, N. C., Gelatin-polycaprolactone-nanohydroxyapatite electrospun nanocomposite scaffold for bone tissue engineering. *Materials science & engineering. C, Materials for biological applications* **2021,** DOI: 10.1016/j.msec.2020.111588.
115. Rabel, K.; Kohal, R. J.; Steinberg, T.; Rolauffs, B.; Adolfsson, E.; Altmann, B., Human osteoblast and fibroblast response to oral implant biomaterials functionalized with non-thermal oxygen plasma. *Sci Rep* **2021,** DOI: 10.1038/s41598-021-96526-x.
116. Vega, S. L.; Arvind, V.; Mishra, P.; Kohn, J.; Murthy, N. S.; Moghe, P. V., Substrate micropatterns produced by polymer demixing regulate focal adhesions, actin anisotropy, and lineage differentiation of stem cells. *Acta biomaterialia* **2018,** *76*, 21-28.
117. Haas, J.; Ulrich, F.; Hofer, C.; Wang, X.; Braun, K.; Meyer, J. C., Aligned Stacking of Nanopatterned 2D Materials for High-Resolution 3D Device Fabrication. *ACS Nano* **2022,** *16* (2), 1836-1846.
118. Uchida, E.; Uyama, Y.; Ikada, Y., Surface graft polymerization of ionic monomers onto poly(ethylene terephthalate) by UV-irradiation without degassing. *Journal of Applied Polymer Science* **1993,** *47* (3), 417-424.
119. Aor, B.; Khan, I.; Glinel, K.; Jonas, A. M.; Demoustier-Champagne, S.; Durrieu, M.-C., Microchannel Molding Combined with Layer-by-Layer Approach for the Formation of Three-Dimensional Tube-like Structures by Endothelial Cells. *ACS Applied Bio Materials* **2020,** *3* (3), 1520-1532.
120. Boudaoud, A.; Burian, A.; Borowska-Wykręt, D.; Uyttewaal, M.; Wrzalik, R.; Kwiatkowska, D.; Hamant, O., FibrilTool, an ImageJ plug-in to quantify fibrillar structures in raw microscopy images. *Nature Protocols* **2014,** *9* (2), 457-463.